The Astrophysical Journal, 701:428–453, 2009 August 10 doi:10.1088/0004-637X/701/1/428

THE *SPITZER* DEEP, WIDE-FIELD SURVEY

M. L. N. Ashby[1], D. Stern[2], M. Brodwin[1,22], R. Griffith[2], P. Eisenhardt[2], S. Kozłowski[3], C. S. Kochanek[3,4], J. J. Bock[5], C. Borys[5], K. Brand[6], M. J. I. Brown[7], R. Cool[8], A. Cooray[9], S. Croft[10], A. Dey[11], D. Eisenstein[12], A. H. Gonzalez[13], V. Gorjian[2], N. A. Grogin[6], R. J. Ivison[14,15], J. Jacob[2], B. T. Jannuzi[11], A. Mainzer[2], L. A. Moustakas[2], H. J. A. Röttgering[16], N. Seymour[17], H. A. Smith[1], S. A. Stanford[18], J. R. Stauffer[19], I. Sullivan[6], W. van Breugel[20], S. P. Willner[1], and E. L. Wright[21]

[1] Harvard-Smithsonian Center for Astrophysics, 60 Garden St., Cambridge, MA 02138, USA; mashby@cfa.harvard.edu
[2] Jet Propulsion Laboratory, California Institute of Technology, Pasadena, CA 91109, USA
[3] Department of Astronomy, The Ohio State University, Columbus, OH 43210, USA
[4] The Center for Cosmology and Astroparticle Physics, The Ohio State University, Columbus, OH 43210, USA
[5] California Institute of Technology, Pasadena, CA 91125, USA
[6] Space Telescope Science Institute, Baltimore, MD 21218, USA
[7] School of Physics, Monash University, Clayton 3800, Victoria, Australia
[8] Department of Astrophysical Sciences, Princeton University, Princeton, NJ 08544, USA
[9] University of California, Irvine, CA 92697, USA
[10] University of California, Berkeley, CA 94720, USA
[11] NOAO, 950 N. Cherry Ave., Tucson, AZ 85719, USA
[12] Steward Observatory, Tucson, AZ 85721, USA
[13] Department of Astronomy, University of Florida, Gainesville, FL 32611, USA
[14] UK Astronomy Technology Centre, Royal Observatory, Blackford Hill, Edinburgh EH9 3HJ, UK
[15] Institute for Astronomy, University of Edinburgh, Blackford Hill, Edinburgh EH9 3HJ, UK
[16] Leiden Observatory, Leiden University, P.O. Box 9513, 2300 RA Leiden, The Netherlands
[17] Mullard Space Science Laboratory, University College London, Holmbury St. Mary, Dorking, Surrey RH5 6NT, UK
[18] University of California, Davis, CA 95616, USA
[19] *Spitzer* Science Center, California Institute of Technology, Pasadena, CA 91125, USA
[20] University of California, Merced, CA 95344, USA
[21] University of California, Los Angeles, CA 90095-1562, USA
Received 2009 February 3; accepted 2009 June 1; published 2009 July 23

ABSTRACT

The *Spitzer* Deep, Wide-Field Survey (SDWFS) is a four-epoch infrared survey of 10 deg^2 in the Boötes field of the NOAO Deep Wide-Field Survey using the IRAC instrument on the *Spitzer Space Telescope*. SDWFS, a *Spitzer* Cycle 4 Legacy project, occupies a unique position in the area-depth survey space defined by other *Spitzer* surveys. The four epochs that make up SDWFS permit—for the first time—the selection of infrared-variable and high proper motion objects over a wide field on timescales of years. Because of its large survey volume, SDWFS is sensitive to galaxies out to $z \sim 3$ with relatively little impact from cosmic variance for all but the richest systems. The SDWFS data sets will thus be especially useful for characterizing galaxy evolution beyond $z \sim 1.5$. This paper explains the SDWFS observing strategy and data processing, presents the SDWFS mosaics and source catalogs, and discusses some early scientific findings. The publicly released, full-depth catalogs contain 6.78, 5.23, 1.20, and 0.96×10^5 distinct sources detected to the average 5σ, $4''$-diameter, aperture-corrected limits of 19.77, 18.83, 16.50, and 15.82 Vega mag at 3.6, 4.5, 5.8, and 8.0 μm, respectively. The SDWFS number counts and color–color distribution are consistent with other, earlier *Spitzer* surveys. At the 6 minute integration time of the SDWFS IRAC imaging, $>$ 50% of isolated Faint Images of the Radio Sky at Twenty cm radio sources and $>$ 80% of on-axis XBoötes sources are detected out to 8.0 μm. Finally, we present the four highest proper motion IRAC-selected sources identified from the multi-epoch imaging, two of which are likely field brown dwarfs of mid-T spectral class.

Key words: infrared: galaxies – infrared: stars – surveys

Online-only material: machine-readable tables

1. INTRODUCTION

In 2003, the IRAC Shallow Survey (ISS; Eisenhardt et al. 2004) mapped 8.5 deg^2 of the Boötes field of the NOAO Deep Wide-Field Survey (hereafter NDWFS; Jannuzi et al. 1999). The ISS traced the evolution and clustering of massive galaxies (Brand et al. 2006; Brown et al. 2007, 2008; White et al. 2007), detected thousands of active galaxies (Stern et al. 2005; Desai et al. 2008) and nearly 100 galaxy clusters at $z > 1$ (Stanford et al. 2005; Brodwin et al. 2006; Elston et al. 2006; Eisenhardt et al. 2008), empirically extended low-resolution galaxy templates out to 10 μm (Assef et al. 2008), defined the mid-infrared (mid-IR) galaxy luminosity functions for the local universe (Huang et al. 2007; Dai et al. 2009), and identified rare objects ranging from a radio-loud quasar at $z = 6.12$ to a T4.5 field brown dwarf (Stern et al. 2007). With a mere 90 s per pointing, this survey detected over 350,000 sources in the mid-IR bands observed by IRAC. These objects have a redshift distribution that spans most of the history of the universe (Brodwin et al. 2006).

Inspired by these successes, we undertook the *Spitzer* Deep, Wide-Field Survey (SDWFS; Figure 1), a 200 hr Cycle 4 *Spitzer* Legacy project. SDWFS re-imaged the same Boötes field three

[22] W. M. Keck Postdoctoral Fellow at the Harvard-Smithsonian Center for Astrophysics.

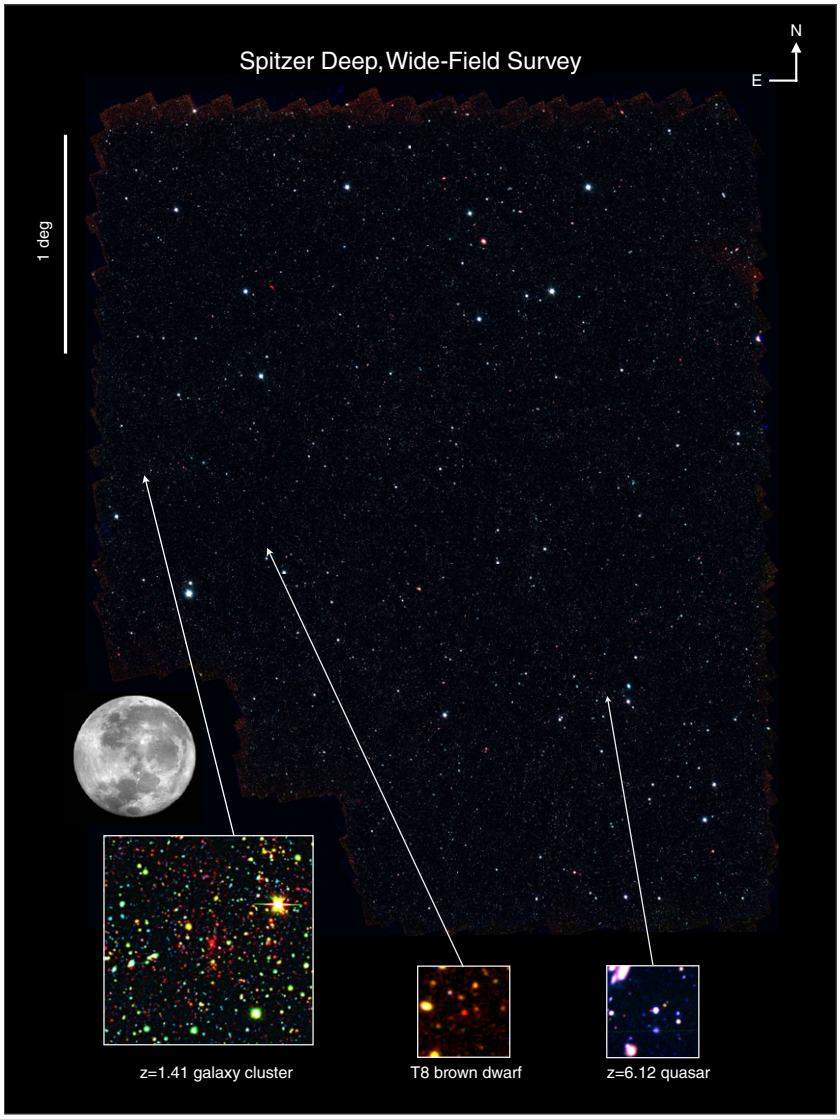

Figure 1. False-color IRAC image of the full SDWFS field using the full, four-epoch data set (RGB = 8.0, 4.5, 3.6 μm). The full Moon is shown to indicate the angular scale. Three interesting targets identified from their IRAC properties are indicated: a spectroscopically confirmed galaxy cluster at $z = 1.41$ (Stanford et al. 2005; $7' \times 7'$; RGB = 4.5 μm, I, B_W), a very late-type, field brown dwarf (P. R. Eisenhardt et al. 2009, in preparation; $1' \times 1'$; RGB = 4.5, 3.6 μm, J), and a radio-loud quasar at $z = 6.12$ (Stern et al. 2007; McGreer et al. 2006; $1' \times 1'$; RGB = I, R, B_W). The galaxy cluster was the most distant known when first identified from the first epoch of SDWFS data. The brown dwarf is amongst the 10 coldest known. The quasar was the first non-SDSS quasar identified at $z > 6$ and is the most distant radio-loud source currently known.

more times during 2007–2008 to the same depth at each epoch as the original ISS. The final SDWFS survey, doubling the photometric depth of the original survey, occupies a unique position in area-depth space relative to previous *Spitzer* projects (Figure 2) and will be valuable for scientific investigations ranging from probing the diffuse background from primordial galaxies to identifying the coldest Galactic brown dwarfs. By cadencing the IRAC observations, SDWFS has also opened the largely unexplored territory of mid-IR variability, a powerful tool for identifying and studying active galaxies. A program of this breadth has a wide range of astronomical uses. Below we highlight four of the key investigations that motivated the SDWFS project. Future papers will describe each of these in more detail, but meanwhile we have made the data set public and describe the potential herein.

Diffuse infrared background from Population III stars. While the first galaxies cannot be individually detected with current instruments, the ensemble of primordial galaxies produces a diffuse extragalactic background, most prominently at near-infrared wavelengths. This background, which directly probes the earliest phases of star formation in the universe, has a distinct angular power spectrum that peaks at scales $\ell \approx 1500 \approx 7\farcm5$ (Cooray et al. 2004). The background also has a distinct spectral energy distribution (SED), falling sharply shortward of redshifted Lyα ($\lambda_{\rm obs} \approx 1.3$–$2.6\,\mu$m). Analyzing data from narrow ($\sim 10' \times 10'$), deep *Spitzer* fields, Kashlinsky et al. (2005, 2007) reported detection of background fluctuations from first-light galaxies at 3.6–4.5 μm. These exciting, yet controversial, results have profound cosmological implications and have generated significant attention both in the press and in the astronomical community. In particular, there is concern that a significant fraction of the reported background is due to faint foreground sources, just below the point-source detection level (Cooray et al. 2007; Sullivan et al. 2007). The SDWFS data set explores an ideal depth and area combination for removing the signal from local galaxy correlations from fluctuation maps (Bock et al. 2006). A fundamental limitation of deep fields for studies of primordial galaxy background fluctuations is that they

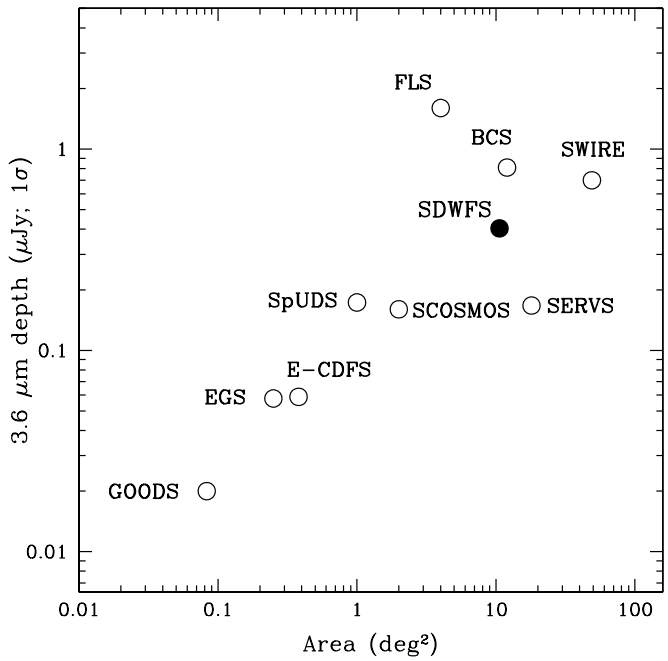

Figure 2. Comparison of SDWFS 3.6 μm depth and total area to the major *Spitzer*/IRAC extragalactic surveys, including GOODS (Great Observatories Origins Deep Survey), EGS (Extended Groth Strip), E-CDFS (Extended Chandra Deep Field South), SpUDS (*Spitzer* Public Legacy Survey of UKIDSS Ultra-Deep Survey), SCOSMOS (*Spitzer* Deep Survey of HST COSMOS 2-Degree ACS Field), SERVS (*Spitzer* Extragalactic Representative Volume Survey), BCS (Blanco Cluster Survey), SWIRE (*Spitzer* Wide-area Infrared Extragalactic Survey), and FLS (*Spitzer* First-Look Survey). All depths are SENS-PET 1σ point-source sensitivities calculated under low background conditions, except for the FLS and SCOSMOS, which assume medium backgrounds. All surveys are contiguous except SWIRE and SERVS, which are divided into six and five subfields, respectively. SDWFS is the only four-band, four-epoch wide-area *Spitzer* survey, thus enabling unique variability studies.

are only two to three IRAC pointings across, and therefore probe only $\ell \gtrsim 10^4$. SDWFS, with its wide-area, shallow coverage, is better suited for studying the diffuse background because it probes the first-galaxy fluctuation spectrum on *both* sides of its predicted $\ell \approx 1500$ peak. Deep observations are not essential: SDWFS is sensitive to Population III background fluctuation levels a factor of 20 fainter than claimed by Kashlinsky et al. (2005), and even pessimistic models suggest fluctuations must exist at these levels (Cooray et al. 2004).

Galaxy clustering at 0.5 < z < 2.5. The growth of galaxies is one of the most challenging problems in modern astronomy. A red sequence of early-type galaxies, with negligible rates of ongoing star formation, is already in place by $z = 1.4$ (e.g., Stanford et al. 2005). Despite having little star formation, the stellar mass within the red galaxy population increases by a factor of 2 or more between $z \sim 1$ and $z \sim 0$, presumably due to the truncation of star formation in blue galaxies (e.g., Bell et al. 2004; Brown et al. 2007; Faber et al. 2007). Where and why this occurs is unclear. Cold dark matter models predict rapid growth of massive dark matter halos, even at late times ($z < 1$). However, observations show that the most massive galaxies grow slowly at late times compared to lower-mass galaxies (e.g., Bundy et al. 2006), a phenomenon commonly referred to as "downsizing." To accurately measure how rapidly massive galaxies grow, one needs large volumes to measure the space density of galaxies with a precision of 10% or better. One can then determine how galaxies are growing relative to their host dark matter halos by measuring their clustering. As the evolving space density and clustering of dark matter halos are accurately modeled by analytic approximations and simulations, one can use the observed space density and clustering of galaxies to determine how galaxies populate dark matter halos (e.g., Zehavi et al. 2005). White et al. (2007) used the original Boötes field data to show that the evolving clustering of galaxies is inconsistent with passive models where massive galaxies do not merge over cosmic time. Brown et al. (2008) used the space density and clustering of galaxies to show that, at late times, massive galaxies grow slowly relative to their host dark matter halos, in part because much of the stellar mass within these halos resides within satellite galaxies. The deeper SDWFS data will improve the photometric redshifts for galaxies out to $z \sim 2.5$, allowing the extension of these studies to the epoch where the global star formation rate peaks. Furthermore, the deeper SDWFS data should result in the detection of 10 clusters with halo masses of 10^{14} $M_\odot$ or more at $z > 1.5$. These may be the environments in which the first red galaxies formed. Will these clusters contain massive galaxies, or will we see evidence for the cluster galaxies growing hierarchically from $z \sim 2$ until the present day?

IRAC studies of active galactic nuclei (AGNs) and AGN variability. The primary goals of the Boötes AGN effort include studying the full (X-ray to radio) SEDs of AGN (e.g., Hickox et al. 2007; Gorjian et al. 2008; Higdon et al. 2008), to determine the infrared luminosity functions of quasars (e.g., Brown et al. 2006), to study the physics of AGN with less sensitivity to selection effects such as dust extinction (e.g., Stern et al. 2005), to examine the distribution of AGN Eddington ratios (Kollmeier et al. 2006), and to probe the relation of AGN to their large-scale environments (e.g., Galametz et al. 2009). In particular, AGNs are known to exhibit photometric variability throughout the electromagnetic spectrum. By cadencing the IRAC observations over multiple visibility windows, SDWFS has opened the largely unexplored territory of mid-IR variability. Dramatic AGN variations have been seen at X-ray, optical, near-infrared, and radio wavelengths (e.g., Hovatta et al. 2008; Papadakis et al. 2008; Sarajedini et al. 2006). Monitoring campaigns are an efficient method to identify AGN and provide information on the size scales, geometries, and physics of the nuclear regions, providing fundamental tests of unified AGN models. The challenges of ground-based mid-IR astronomy, however, have largely restricted infrared variability studies to low-luminosity, nearby sources. One study found variability in most (39/41) sources, with variability most apparent at longer wavelengths (Glass 2004). The wide-area, shallow SDWFS program is the ideal exploratory probe to identify the brightest, most variable infrared sources for detailed study and multiwavelength monitoring while mid-IR capabilities are still available.

The coldest brown dwarfs. One of the most important observational topics in the field of substellar objects is the detection and characterization of objects cooler than T dwarfs—the so-called Y dwarfs, cooler than about 700 K. Such objects must exist because brown dwarfs with inferred masses down to ≈ 5 $M_{\rm Jup}$ have been identified in star-forming regions. According to theoretical models, dwarfs less massive than 30 $M_{\rm Jup}$ with ages > 4 Gyr should have $T < 600$ K, but none has yet been found. This is primarily because their SEDs peak at ≈ 4.5 μm (e.g., Burrows et al. 2003), making them very faint at ground-based optical through near-infrared wavelengths. For instance, while a 600 K brown dwarf could be detected by the Two Micron All Sky Survey (2MASS; Skrutskie et al. 2006) only if closer

Table 1
SDWFS Observations of the Boötes Field

Epoch	Observation Dates	PID	Pipeline Version	No. of BCDs
1	2004 Jan 10–14	30[a]	16.1.0	17014
2	2007 Aug 8–13	40839	16.1.0	19956
3	2008 Feb 2–6	40839	17.0.4	20200
4	2008 Mar 6–10	40839	17.0.4	20680

Note. [a] The IRAC Shallow Survey, Eisenhardt et al. (2004).

than 1 pc, it would be detectable in a single SDWFS epoch out to almost 50 pc at 4.5 μm. Moreover, the multi-epoch SDWFS survey can detect the proper motion of any dwarf with tangential velocity >20 km s^{-1} out to 50 pc. The models of Martín et al. (2001) predict that about 10% of brown dwarfs should be of type Y. SDWFS ought to detect $\approx$ 5 brown dwarfs cooler than 1400 K, and there is a reasonable chance of detecting a Y dwarf. Our multi-epoch survey will thus provide a systematic census of faint brown dwarfs. We have already confirmed one T4.5 brown dwarf from the original ISS (Stern et al. 2007), and we have identified four additional mid-T brown dwarf candidates based on proper-motion measurements in the SDWFS data set (Section 4.6). A sample of cooler brown dwarf candidates, later than approximately T7, has recently been identified from the full SDWFS data set (P. R. Eisenhardt et al. 2009, in preparation). Including the optical data, the Boötes field's 13-yr baseline will also provide a long lever arm for proper-motion studies of other (less red) Galactic populations.

1.1. The Boötes Field

Much as the Great Observatory Origins Deep Survey (GOODS; Giavalisco et al. 2004) fields have become the fields of choice for ultradeep pencil-beam surveys across the electromagnetic spectrum, the 9 deg^2 Boötes field has become the wide-area, deep survey field of choice and thus was chosen as the target field for SDWFS. Motivated by its low Galactic background and high ecliptic latitude, various teams have mapped the entire field at X-ray wavelengths with *Chandra* (Murray et al. 2005; Kenter et al. 2005; Brand et al. 2006), at ultraviolet wavelengths with *Galaxy Evolution Explorer* (*GALEX*; Hoopes 2004), at optical/near-infrared wavelengths from NOAO (Jannuzi et al. 1999; Elston et al. 2006), at mid-IR wavelengths with *Spitzer* (Eisenhardt et al. 2004; Soifer et al. 2004), and at radio wavelengths from the Very Large Array (VLA) and Westerbork at 20, 90, and 200 cm (de Vries et al. 2002; Croft et al. 2004, 2008). Over 20,000 spectroscopic redshifts in Boötes have been obtained, the majority from the AGN and Galaxy Evolution Survey (AGES; C. S. Kochanek et al. 2009, in preparation), and the field is also the target of both ongoing and future surveys, such as deeper near-infrared imaging with the NEWFIRM camera on the Kitt Peak 4 m (led by SDWFS co-investigator Gonzalez), 850 μm imaging with SCUBA2, a far-infrared guaranteed-time (GTO) survey with *Herschel*, near-infrared imaging with the CIBER rocket experiment in Spring 2009 (led by SDWFS co-investigator Bock), and hard X-ray (6–79 keV) imaging with the *Nuclear Spectroscopic Telescope Array* (*NuSTAR*), scheduled for launch in 2011. Most of these multiwavelength data are (or will be) public, and over 80 refereed papers have been published from the Boötes surveys.[23]

This paper is organized as follows: Section 2 discusses the details of the SDWFS observing strategy and data reduction, and Section 3 describes the source identification, astrometric verification, and photometry. Section 4 presents preliminary results from the analysis of the SDWFS data, including mid-IR number counts, color distributions, and identification fractions for both radio and X-ray sources. Section 5 summarizes these results. Unless otherwise stated, all magnitudes are in the Vega system.

[23] http://www.noao.edu/noao/noaodeep/ndwfspublications.html

2. OBSERVATIONS AND DATA REDUCTION

2.1. Mapping Strategy

The SDWFS observing campaign consisted of four co-extensive surveys of the 8.5 deg^2 Boötes field, carried out over roughly 4 yr (Table 1). The first visit to the field occurred close to the start of the *Spitzer* mission, in 2004 January, as part of a guaranteed time program led by the IRAC instrument team. This program was called the ISS (PID 30; Eisenhardt et al. 2004) and has had numerous successes, as discussed Section 1. A subsequent visit as part of the SDWFS program in 2007 August remapped the same region to the same depth, and the final two visits, again to the same depth, were at the beginning and end of the following visibility window (2008 February and March). Together, these four observations provide temporal intervals of 1 month, 6 months, and 3.5 yr between visits (Table 1). We refer to each of these four Boötes campaigns as an "epoch," with the original ISS now considered "epoch one" of SDWFS.

The observing strategy was optimized to maximize the reliability of the data taken within single epochs. During each of the campaigns, the entire Boötes field was observed to a depth of 90 s per sky position. The field was split into 15 "groups," each consisting of three co-extensive Astronomical Observing Requests (AORs). On average, each group covered approximately 45′ × 45′, or 9 × 9 IRAC pointings. In practice, group size and shape varied because of the gerrymandering needed to fit groups to the chevron shape of the existing optical/near-infrared coverage of the NDWFS.

To ensure that flux from asteroids could later be reliably masked and excluded from the SDWFS mosaics, each group was observed in three passes of 30 s depth, with each pass of each group constituting a separate AOR. The 30 s frame time provided background-limited or nearly background-limited data in all four IRAC bands and ensured that dithering overheads did not dominate the AOR execution time. The time required to obtain a single 30 s pass on a group ensured gaps of at least 2 hr between observations of each sky position. For typical asteroid motions of 25″ hr^{-1}, asteroids moved by $\approx$ 1′ between maps. Since this is much smaller than a typical map width, this mapping strategy reliably tracks asteroid motions, thus providing both a clean, final mosaic for Galactic and extragalactic studies and a scientifically valuable asteroid sample at high ecliptic latitude.

Our mapping strategy incorporated several elements to facilitate self-calibration of the data by maximizing interpixel correlations (e.g., Arendt et al. 2000). We *dithered* the observations on small scales and *offset* by one-third of an IRAC field of view between successive passes through each group. This provided interpixel correlation information on both small and large scales. In addition, for AOR groups having rectangular shapes, we *cadenced* the observations such that revisits cover the same area but with a different step size. For example, a group that imaged a 40′ × 60′ region using an 8 × 12 grid map with

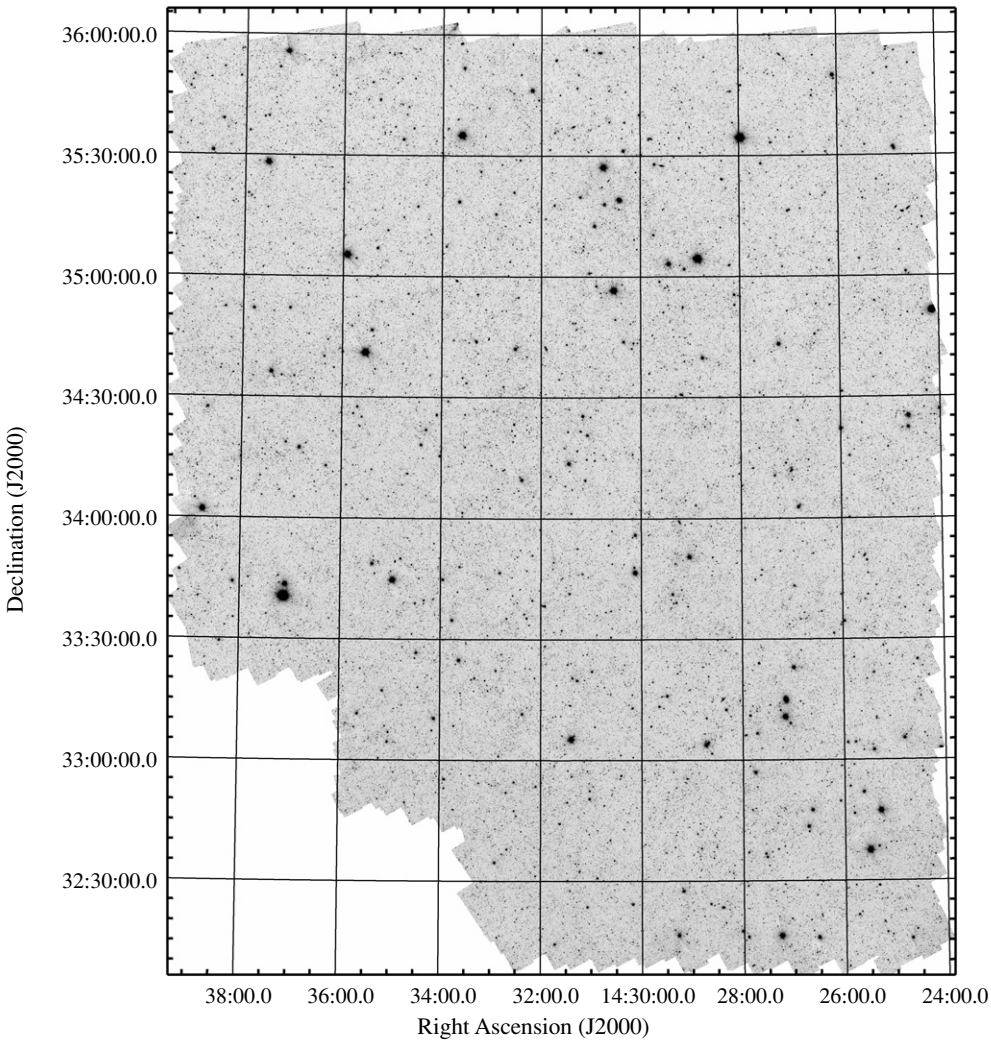

Figure 3. Total SDWFS IRAC 3.6 μm co-add (four co-added epochs) of the Boötes field.

290″ step size subsequently used 9 × 12 and 8 × 13 grid maps (with suitably scaled down step sizes). With a $\lesssim$ 10% penalty in mapping efficiency, cadencing significantly enhances the interpixel correlations across all scales and greatly increases the redundancy of the data sets. Finally, by reobserving the field multiple times at different roll angles and different times, our observing strategy is very robust against bad rows and columns, large-scale cosmetic defects on the array, glints, changes in the zodiacal background, after images resulting from saturation due to bright stars, variations in the zero level, and the color dependence of the IRAC flat field across the array (Hora et al. 2008). In particular, the challenging diffuse background measurements, one of the key goals of the SDWFS project (e.g., Sullivan et al. 2007), are vastly aided by the redundant coverage: independent data sets are the best way to assess many systematic errors. The final SDWFS coverage is 3 × 30 s for each epoch and 12 × 30 s for the complete survey. The number of exposures needed to cover the field in a single epoch varied from 17,014 to 20,680, depending on roll angle. The full, co-added SDWFS 3.6 μm map is presented in Figure 3, and the corresponding coverage map is presented in Figure 4. Figure 5 illustrates how the source density changes through the IRAC bands at the full SDWFS depths. Figure 6 presents the cumulative area coverage as a function of exposure time.

2.2. Data Reduction

The data reduction was based on the IRAC Basic Calibrated Data (BCD). The 3.6, 5.8, and 8.0 μm BCD frames were object masked and median stacked on a per-AOR basis; the resulting stacked images were visually inspected and subtracted from individual BCDs within each AOR to eliminate long-term residual images arising from prior observations of bright sources. This was not necessary for the 4.5 μm BCDs because the 4.5 μm IRAC detector array does not suffer from residual images.

The first two epochs were processed with pipeline version 16.0.1. The 3.6 and 4.5 μm BCDs were examined by hand and modified using custom software routines to correct column pulldown and multiplexer bleed effects associated with bright sources. Much of this software is available from the *Spitzer* Science Center[24] and is based on algorithms designed and coded by SDWFS co-I's. The last two epochs were processed with pipeline version 17.0.4. For these, we used the so-called corrected BCD frames, in which the BCD pipeline automatically applies multiplexer bleed and column pulldown corrections. The photometric calibrations are identical for both pipelines.

After these preliminaries, the data were mosaiced into eight overlapping subfields (tiles), each slightly larger than a degree

[24] http://ssc.spitzer.caltech.edu/archanaly/contributed/browse.html

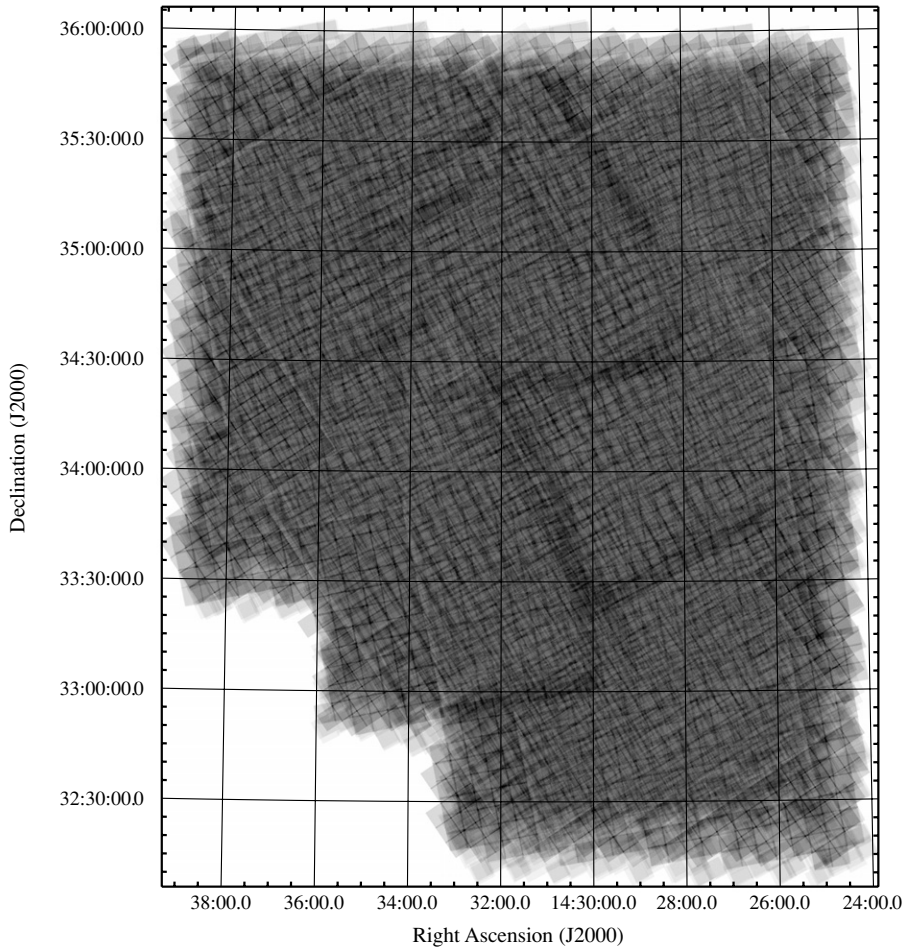

Figure 4. Total SDWFS IRAC 3.6 μm coverage map (four co-added epochs) illustrating the uniformity of depth over the Boötes field. The coverage ranges from a maximum of 19 × 30 s (black) in the interior to no coverage (white), at the edge. The total area observed with at least one 30 s exposure is 10.6 deg^2. The total area covered by the other three IRAC bands is nearly identical, but the coverage differs in detail at the edges of the field because the 3.6/5.8 μm and 4.5/8.0 μm fields of view are offset from each other.

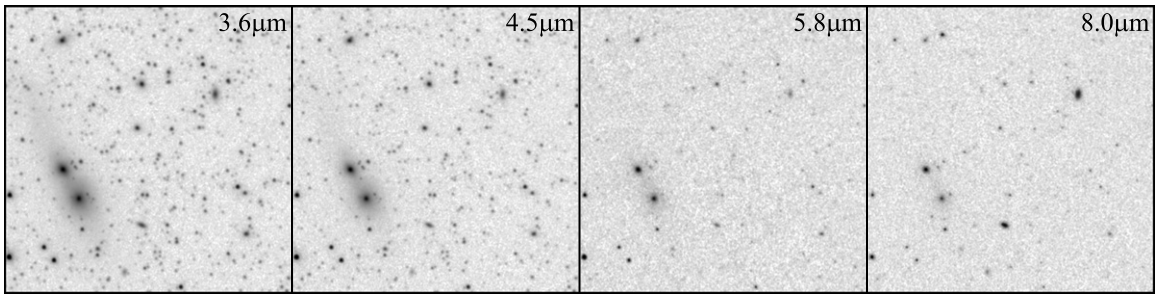

Figure 5. Montage of cutouts from the four-epoch 12 × 30 s mosaics of the Boötes survey field, illustrating the source densities in the IRAC bands. Coverage is roughly 5′ × 5′, centered at $(\alpha, \delta)_{J2000}$ = (14:31:48,+34:43:00). North is up, and east is to the left. The two relatively bright galaxies in the east half of the frame are an interacting pair of red elliptical galaxies. They were presented as evidence of "dry merging" in van Dokkum (2005; galaxies 17-596 and 17-681 in Figures 3(a) and 4(a)).

across, using IRACproc (Schuster et al. 2006). In order to take advantage of the subpixel shifts of our mapping strategy, the mosaics were resampled to 0.″84 per pixel, so that each mosaic pixel subtends half the area of the native IRAC pixel. IRACproc augments the capabilities of the standard IRAC reduction software (MOPEX). The software was configured to automatically flag and reject cosmic ray hits based on pipeline-generated masks together with a sigma-clipping algorithm for spatially coincident pixels. IRACproc calculates the spatial derivative of each image and adjusts the clipping algorithm accordingly. Thus, pixels where the derivative is low (in the field) are clipped more aggressively than are pixels where the spatial derivative is high (point sources). This avoids downward biasing of point-source fluxes in the output mosaics. For the final, total co-add (12 × 30 s) of all four epochs, we proceeded in the same manner as for the individual epochs with the minor change that only temporal outlier rejection was performed.

For both the single epoch and the total co-adds, the outlier rejection threshold was iteratively refined by inspecting difference images (Section 4.6): we subtracted successive epochs from each other to suppress emission from the non-varying celestial sources (i.e., almost all of them), so that cosmic

Table 2
SExtractor Parameter Settings

Parameter	3.6 μm	4.5 μm	5.8 μm	8.0 μm
DETECT_MINAREA (pixel)	3	3	4	4
FILTER	gauss_2.0_5x5	gauss_2.0_5x5	gauss_2.0_5x5	gauss_2.5_5x5
DEBLEND_MINCONT	0.00005	0.00005	0.0001	0.0001
SEEING_FWHM (arcsec)	1.66	1.72	1.88	1.98

Notes. Parameter settings used identically in all four IRAC bands were DETECT_THRESH=1.5, DEBLEND_NTHRESH=64, BACK_SIZE=256, BACK_FILTERSIZE=3, BACKPHOTO_TYPE=GLOBAL, and WEIGHT_TYPE=MAP_WEIGHT.

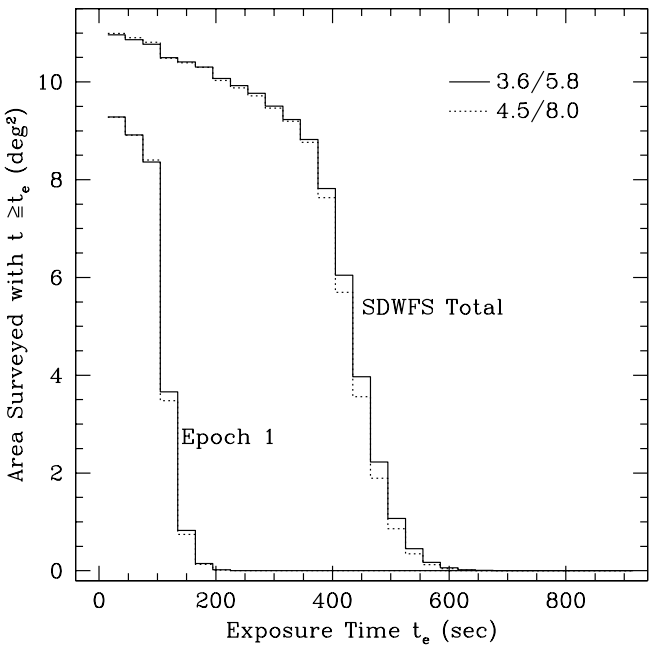

Figure 6. Cumulative area coverage as a function of exposure time for IRAC observations of the Boötes survey field. The median coverage obtained in a single epoch and the full survey is about 90 and 420 s, respectively, in all bands.

ray artifacts became obvious against the dramatically flattened background.

Each tile was reduced independently of all other tiles. IRACproc automatically identified and incorporated all exposures overlapping the specified field of a given tile into the corresponding mosaic. This inevitably resulted in each tile having some amount of irregular, low-coverage "crust" on its periphery even though the depth of coverage within each tile's analysis region was complete and free of cosmic rays by virtue of the iterated outlier rejection described above. The tiles were subsequently combined into full-field images, one for each band and each epoch, using the Montage toolkit (ver. 3.0; Berriman et al. 2004). The coverage maps were used as a means of preventing the low-coverage peripheral "crusts"—with their relatively high prevalence of cosmic ray hits—from degrading the final mosaics. The outcome was a suite of 20 mosaics: four from each of the four epochs, plus another four for the total 12 × 30 s co-add. These data, including coverage maps and catalogs, are all available from the *Spitzer* Science Center.[25]

3. SOURCE IDENTIFICATION

3.1. Source Extraction and Photometry

The survey depths achieved are well above the confusion limits even when all four epochs are combined into total co-adds

[25] http://ssc.spitzer.caltech.edu/legacy/sdwfshistory.html

Table 3
SDWFS Aperture Corrections

Aperture Diameter	3.6 μm	4.5 μm	5.8 μm	8.0 μm
3″	−0.67	−0.69	−0.89	−1.01
4″	−0.38	−0.40	−0.57	−0.69
5″	−0.24	−0.25	−0.38	−0.51
6″	−0.17	−0.17	−0.26	−0.38

Notes. Corrections (magnitudes) derived from well-detected stars in the full-depth, stacked SDWFS image. The corrections have been added to the corresponding aperture photometry measurements in the SDWFS catalogs to correct them to 24″-diameter apertures, as used for calibration stars.

comprising 12 × 30 s coverage. For this reason, we constructed source catalogs using SExtractor (ver. 2.5.0; Bertin & Arnouts 1996), a standard tool for these purposes. In addition to source catalogs, we also generated both background and object "check images." Inspecting those check images, we iteratively chose parameter settings, ultimately settling on the values listed in Table 2. The outcomes did not depend sensitively on many of the parameters, although the correct choices of convolution filter width and deblending parameters were necessary in order to obtain "object" check images that appeared complete upon inspection. We used the coverage maps as detection weight images in the standard way. Regions covered by fewer than two exposures were excluded using separate "flag" images constructed from the coverage maps.

Photometry was carried out using several approaches available in SExtractor. We compiled fluxes and magnitudes within 10 apertures having diameters from 1″ to 10″ in 1″ increments, plus 15″ and 24″, for 12 apertures in all. We also measured MAG_AUTO magnitudes, for which SExtractor measures sources' fluxes interior to elliptical apertures with sizes and orientations determined using the second-order moments of the light distribution measured above the isophotal threshold.

Having first verified that the astrometry is accurate on scales much smaller than a SDWFS mosaic pixel (Section 3.4), we used SExtractor in dual-image mode to photometer the SDWFS mosaics. In dual-image mode, sources are detected, their centers are located, and their apertures are defined in one image, and subsequently photometry is carried out in another image using those preestablished apertures and source centroids. We used the four-epoch 12 × 30 s mosaics as the detection images in all cases because of their superior noise properties.

SExtractor was configured to define a source as a set of three or more connected pixels each lying 1.5σ above the background. With this parameter setting, we detected a total of 8.2, 6.7, 3.1, and 1.8 × 10^5 sources at 3.6, 4.5, 5.8, and 8.0 μm, respectively, in the four-epoch 12 × 30 s SDWFS mosaics. This corresponds to 1σ depths of 21.7, 20.8, 18.7, and 18.0 Vega mag.

To compensate for flux falling outside the SExtractor apertures, we used the 12-aperture photometry for bright, unre-

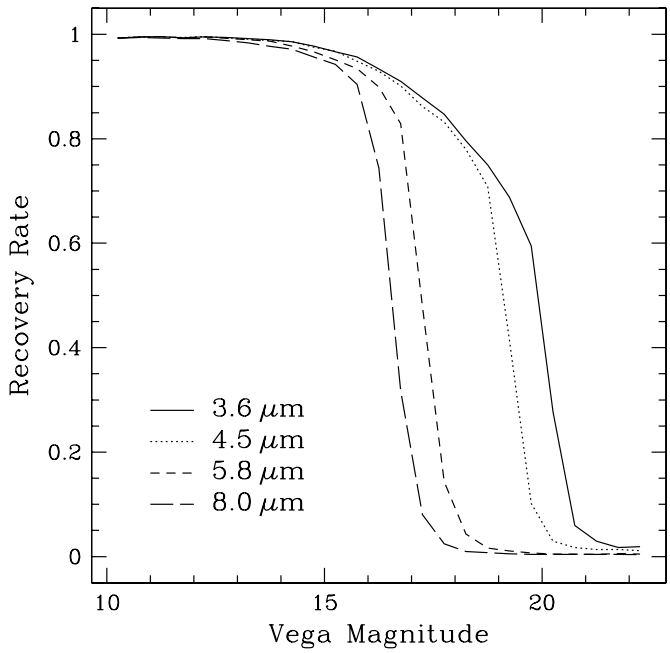

Figure 7. Fraction of simulated point sources recovered as a function of input magnitude for the total co-add of all four IRAC observations of the Boötes survey field.

Table 4
SDWFS Completeness Limits

Completeness Level (%)	3.6 μm	4.5 μm	5.8 μm	8.0 μm
80	18.2	18.1	16.8	16.1
50	19.9	19.1	17.2	16.5

Note. Magnitudes are relative to Vega, and correspond to completeness levels established with the simulations described in Section 3.3.

solved sources in the full-depth, four-epoch mosaics to derive empirical aperture corrections that correct the photometry to 24″-diameter apertures. These aperture corrections are listed in Table 3. Comparing our 5″–24″-diameter aperture corrections to the 4.″9–24.″4-diameter aperture corrections provided in the IRAC Instrument Handbook (ver. 3.0), our corrections are systematically ∼3.5% larger. Besides the slight differences in aperture radii, this difference likely arises from a combination of the slightly different point-spread function (PSF) of our multi-epoch stacked images and differences in how the backgrounds were determined. In particular, stacking multi-epoch data will suppress azimuthal asymmetries such as diffraction spikes, leading to a PSF profile that is more closely circular.

3.2. Completeness and Depth Simulations

The survey completeness in each band was assessed with a standard Monte Carlo approach. Using the IRAF task *noao.artdata.mkobjects*, 10,000 artificial stars in each half-magnitude bin between $10 \leqslant m(\mathrm{IRAC}) \leqslant 22.5$ were added at random positions to the mosaics. Catalogs were extracted from the resulting 25 images in each band exactly as described above. The recovery rates as a function of magnitude in the IRAC bands are plotted in Figure 7. The recovered fraction has a sharp falloff in the relatively sparse, redder bands, while in the deeper 3.6 and 4.5 μm data, the decline is more gradual. This is likely caused by moderate levels of confusion in these more sensitive bands, where the high object density leads to difficulties for object recovery in crowded regions. The 50% and 80% completeness levels are given in Table 4.

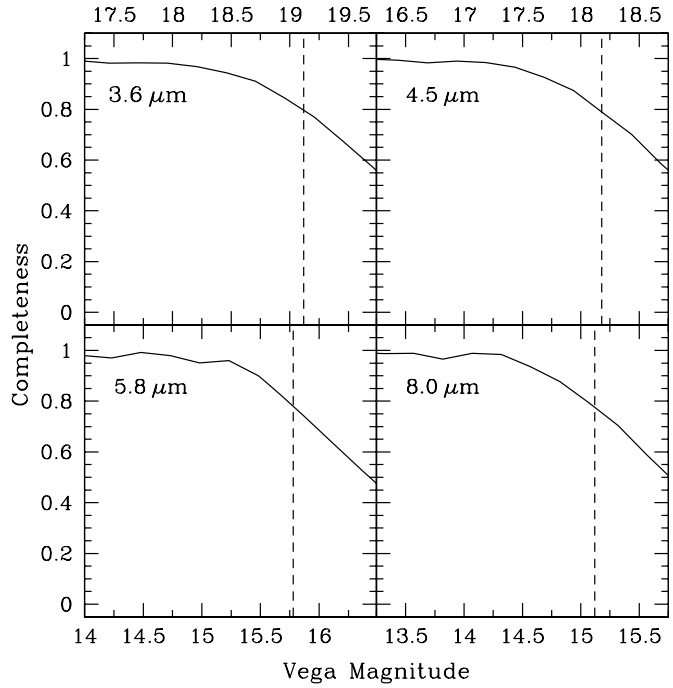

Figure 8. Empirical single-epoch fractional completeness estimates for SDWFS. Each panel shows the fraction of SDWFS sources identified in the total 12×30 s SDWFS co-adds that are also found in the epoch-four 3×30 s co-add. The 5σ sensitivity limits established with the Monte Carlo approach are shown as vertical dashed lines.

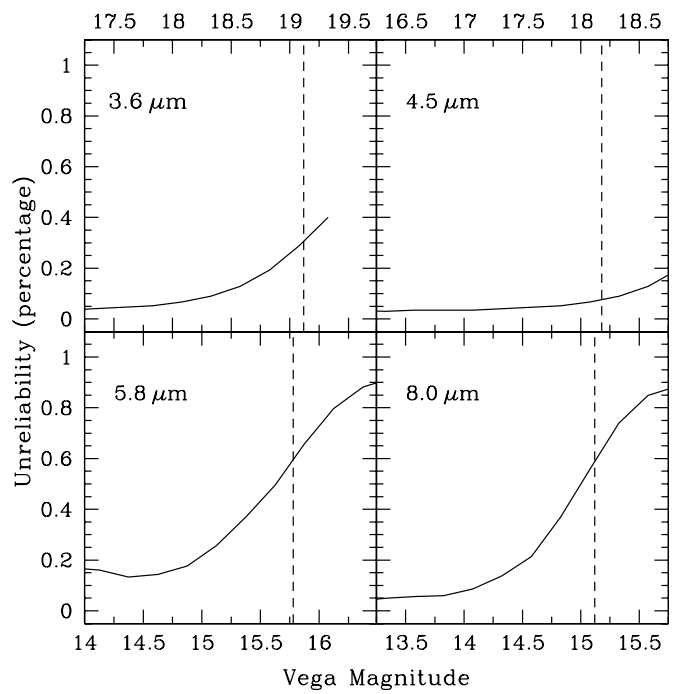

Figure 9. Empirical single-epoch unreliability estimates for SDWFS. Here, unreliability is defined as the percentage of sources detected at 3×30 s (in SDWFS epoch 4) that are *not* found in the deeper 12×30 s SDWFS co-add. The 5σ sensitivity limits established with the Monte Carlo approach are shown as vertical dashed lines. For sources brighter than the 5σ single-epoch sensitivity limits, SDWFS detections are at least 99.4% reliable.

The mosaics' depths were also estimated using Monte Carlo techniques. In all four IRAC bands, 10,000 random positions within the mosaics (both single epoch and SDWFS total) were

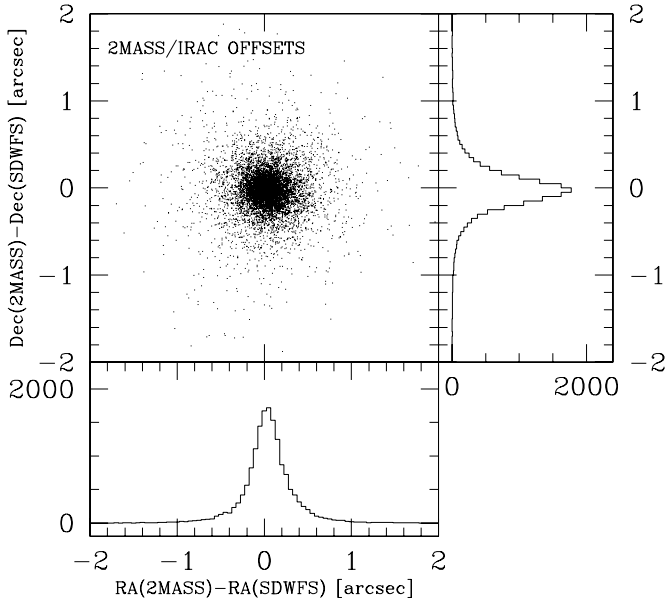

Figure 10. Astrometric offsets (2MASS–SDWFS) between catalog positions drawn from the total IRAC 3.6 μm co-add and positions of all 16,045 2MASS sources that lie in the 10.6 deg^2 region of Boötes covered by SDWFS.

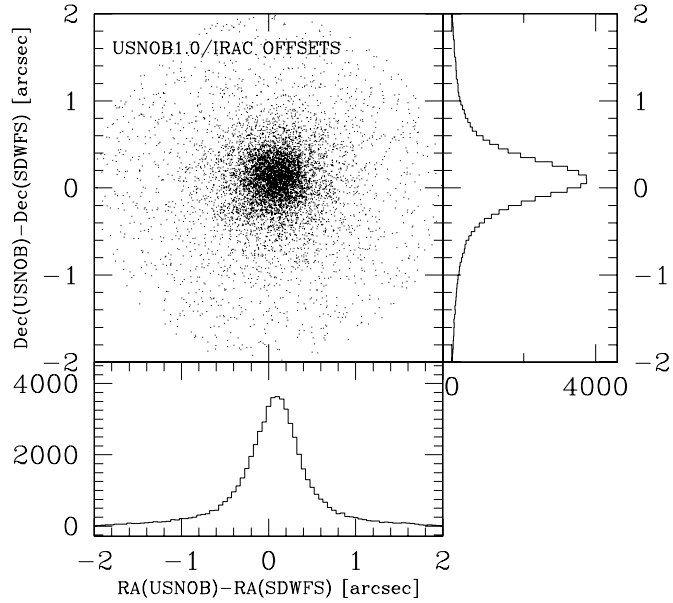

Figure 11. Astrometric offsets (USNOB–SDWFS) between catalog positions drawn from the total SDWFS 3.6 μm co-add and positions of sources in the USNOB1.0 catalog for the 10.6 deg^2 Boötes field. For clarity, the central panel shows only 7500 of the $\sim$56, 700 matches.

photometered in various apertures. Gaussians were fitted to the negative half of the measured surface brightness distributions, which are devoid of any contribution from real sources, in order to reliably estimate sky noise. Table 5 lists the aperture-corrected 5σ depths in several apertures for both the first epoch and the full survey. The single-epoch depths can be a few tenths of a magnitude better than those reported from the original ISS (Eisenhardt et al. 2004), primarily at 3.6 μm. This is attributable to improved processing algorithms. In a corrected 4″-diameter aperture from a single epoch, SDWFS reaches depths of 19.1, 18.2, 15.8, and 15.1 mag in the IRAC bands. The full-depth images reach approximately 0.7 mag deeper.

Single-epoch survey completeness (Figure 8) was estimated by counting the epoch-four detections having 4″-diameter aperture magnitudes that agreed within 0.2 mag with the corresponding detections in the full-depth SDWFS mosaics. The four 3 × 30 s SDWFS catalogs are $\sim$80% complete at the corresponding 5σ sensitivity limits. Single-epoch catalog unreliability (Figure 9) was estimated by computing the percentage of sources in the epoch-four catalog which do *not* appear in the full-depth mosaics. At 3.6 and 4.5 μm, the single-epoch SDWFS catalogs are at least 99.7% and 99.9% reliable at or above the 5σ sensitivity limits. At 5.8 and 8.0 μm, the catalogs are 99.4% reliable at these levels.

3.3. Astrometry

To estimate the accuracy of the astrometry in our SExtractor catalogs, we matched sources selected at 3.6 μm (where IRAC has the highest spatial resolution) to the 2MASS and USNOB 1.0 (Monet et al. 2003) catalogs. Figures 10 and 11 show the results.

Within the 2.″0 matching radius, we matched all 16,045 Boötes 2MASS sources to our IRAC 3.6 μm source list. Given that the SDWFS data are significantly deeper than 2MASS, the 100% match rate was expected. The astrometric agreement is excellent: the mean offsets (2MASS–SDWFS) are 0.″04 and −0.″02 in right ascension and declination, respectively. The corresponding standard deviations of the measured offsets were 0.″3 in both coordinates, consistent with the expected measurement error given the IRAC spatial resolution of 1.″66 (FWHM) and the 0.″84 mosaic pixel size. Given that the *Spitzer*/IRAC pipeline automatically assigns a coordinate solution to individual BCD frames by identifying and referencing the ensemble of all 2MASS stars imaged simultaneously in both IRAC FOVs (the so-called super-boresight calibration), this level of accuracy is unsurprising.

Table 5
5σ SDWFS Depths

Aperture Diameter	3.6 μm	4.5 μm	5.8 μm	8.0 μm
Single epoch				
3″	19.31	18.27	15.88	15.18
4″	19.12	18.18	15.78	15.12
5″	18.91	18.02	15.65	15.00
6″	18.73	17.81	15.52	14.89
Total SDWFS				
3″	19.95	18.98	16.66	15.85
4″	19.77	18.83	16.50	15.82
5″	19.56	18.66	16.37	15.68
6″	19.32	18.49	16.29	15.57

Notes. Magnitudes are relative to Vega. Depths, estimated from the sky noise, are aperture corrected and apply to survey locations having the median exposure times of 90 and 420 s in the single epoch and full-depth SDWFS mosaics, respectively.

An additional, independent estimate of SDWFS astrometric accuracy comes from comparison with USNOB1.0. There appears to a small but systematic coordinate offset between SDWFS sources and those tabulated in USNOB1.0. Median offsets (USNOB–SDWFS) are 0.″06 and 0.″08 in right ascension and declination, respectively, as shown in Figure 11. The dispersion of offsets is larger than for 2MASS, 0.″5 standard deviation in each coordinate. Thus, the astrometric agreement of all three catalogs is excellent overall, but there is a slight offset between 2MASS and SDWFS relative to USNOB1.0 in this region of sky. The magnitude of the discrepancy is somewhat

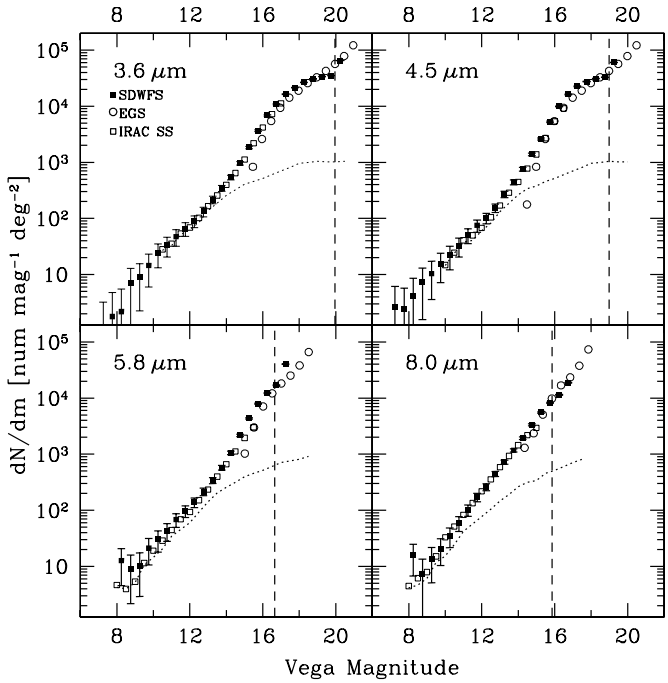

Figure 12. Differential source counts for SDWFS. The solid squares show the total counts (stars+galaxies) drawn from the full-depth SDWFS mosaic. The open squares are the source counts originally measured for the IRAC Shallow Survey (the first SDWFS epoch) by Fazio et al. (2004). The open circles indicate the counts tabulated in the deep IRAC survey of the Extended Groth Strip by Barmby et al. (2008). The dotted lines indicate star counts corresponding to point sources based on a Galactic model (tabulated by Fazio et al. 2004). All counts plotted have been corrected for incompleteness using the results of the simulations described in Section 3.3. The vertical dashed lines indicate the 5σ sensitivity limits corresponding to 3″-diameter apertures (Table 5).

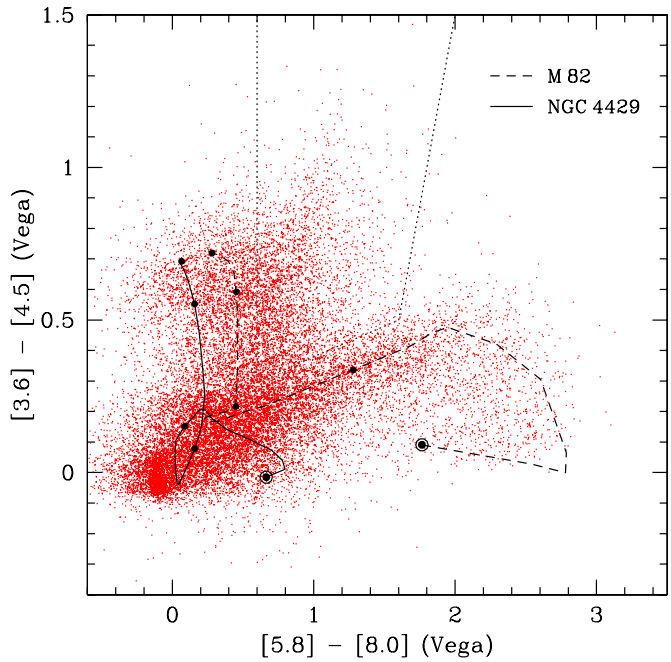

Figure 13. IRAC color–color diagram for 20,000 randomly selected SDWFS sources detected at 5σ significance or greater (red dots). All photometry shown derives from 3″-diameter aperture magnitudes, corrected uniformly to 12 pixel radius magnitudes (24″). The $z \leqslant 2$ color tracks of two non-evolving galaxy templates (Devriendt et al. 1999) are shown: the quiescent S0/Sa galaxy NGC 4429 (solid line) and the nearby starburst M82 (dashed line). The solid dots correspond to $z = 0.5$, 1.0, 1.5, and 2.0, and the dot-in-circles indicate $z = 0$. The dotted line defines a region of this color–color space that is known to be occupied predominantly by active galaxies (Stern et al. 2005).

smaller than that found between, e.g., zBoötes and NDWFS (0.″2; Figure 4 of Cool 2007).

3.4. SDWFS Catalogs

We merged the single-band source lists by combining the astrometry defined in the "detection" images together with photometry carried out in the "measurement" images. In this way, we created a final set of 20 band-merged catalogs, i.e., for sources selected in each of the four IRAC filters, we merged the four-band photometry from each of the four epochs as well as from the total co-add. Each catalog contains aperture-corrected photometry measured within sets of identical circular apertures having diameters of 4″ and 6″ plus MAG_AUTO.

Depending on the application, it may be advantageous to perform source selection in different bands. For example, selection at 3.6, 4.5, and 8.0 μm might well be optimal for studies of nearby galaxies, for selection of substellar objects, and selection of red, high-redshift objects, respectively. Rather than impose our own selection bias on users of SDWFS data, we make all 20 SDWFS band-matched catalogs available in the electronic edition of this paper. The catalog formats are defined in Tables 6– 25.

4. ANALYSIS

4.1. Confusion

We estimated worst-case confusion arising from *well-detected* sources as follows. SDWFS detected 6.78, 5.23, 1.20, and 0.96×10^5 sources above the aperture-corrected 4″-diameter 5σ thresholds (Table 5) in the full-depth mosaics covering 10.6 deg^2. The source density is greatest at 3.6 μm, roughly 0.008 per 3.6 μm beam (where the beam solid angle Ω was estimated under the assumption that in the four-epoch co-add, the trefoil IRAC PSF has a Gaussian profile with FWHM = 1.″66, so that $\Omega = \pi\sigma^2 = 1.57$ arcsec^2). This implies that fewer than 1% of the 3.6 μm SDWFS sources are confused with other sources that lie above the 3.6 μm detection limit.

We also estimated source confusion arising from *faint* sources by examining the deep 3.6 μm source counts in the IRAC image of the Extended Groth Strip (EGS; Barmby et al. 2008). Specifically, we summed EGS counts in the three half-magnitude bins lying just below the SDWFS 5σ detection limit to arrive at a density of roughly 4.2×10^5 sources deg^{-2} down to 21.7 mag, which corresponds roughly to the 1σ SDWFS limit. This implies that if one extends the counts down to the 1σ level, there are about 0.05 sources per IRAC beam in the four-epoch 3.6 μm SDWFS mosaic. Of course, this estimate slightly underestimates the effects of confusion, because galaxies are clustered rather than randomly distributed, and they are not, in general, point sources. Nonetheless, to a reasonable approximation roughly one out of every 20 SDWFS sources will have 3.6 μm photometry unavoidably contaminated by emission from a faint, overlapping source. The percentage will be smaller at the longer wavelengths. This contamination is of course more significant for fainter sources, and is relatively unimportant for the high-significance detections.

4.2. Number Counts

A fundamental feature of any survey is the relationship it reveals between the fluxes of the objects it detects and their

Table 6
SDWFS Four-Epoch, 3.6 μm-Selected Catalog

R.A., Decl. (J2000)	$m_{4,i}$[a]	$\sigma_{4,i}$[b]	$m_{6,i}$[a]	$\sigma_{6,i}$	MAG_AUTO$_i$	$\sigma_{\mathrm{MAG\_AUTO},i}$	Flags[c]
216.8795190 +32.1472610	17.37 17.10 17.09 15.62	0.03 0.04 0.32 0.19	17.40 17.26 99.00 15.73	0.03 0.07 99.00 0.24	17.47 17.58 99.00 16.61	0.04 0.12 99.00 0.67	0
216.8787756 +32.1490457	19.07 99.00 99.00 99.00	0.12 99.00 99.00 99.00	19.07 99.00 99.00 99.00	0.15 99.00 99.00 99.00	19.14 99.00 17.71 16.12	0.20 99.00 1.07 0.36	0
216.8779087 +32.1508507	19.00 19.10 17.05 99.00	0.11 0.23 0.51 99.00	19.07 20.04 16.61 99.00	0.15 1.19 0.26 99.00	19.23 99.00 16.89 99.00	0.21 99.00 0.38 99.00	0

Notes. The SDWFS full-co-add catalog of sources selected using detection within the total 3.6 μm mosaic. Within each of the sets of four columns (e.g., $m_{4,i}$) the tabulated values correspond to 3.6, 4.5, 5.8, and 8.0 μm, respectively. Entries equal to 99 indicate the source lies below the 5σ detection limit. This printed version is only a sample. All 20 SDWFS catalogs are also available from the *Spitzer* Science Center as ver. DR1.1; they are ver. 3.4 according to the internal SDWFS team documentation.
[a]Aperture corrected to 12″ radius total Vega magnitudes.
[b]Tabulated errors are measurement errors only and do not account for any systematic errors.
[c]SExtractor flag output.
(This table is available in its entirety in a machine-readable form in the online journal. A portion is shown here for guidance regarding its form and content.)

Table 7
SDWFS Four-Epoch, 4.5 μm-Selected Catalog

R.A., Decl. (J2000)	$m_{4,i}$	$\sigma_{4,i}$	$m_{6,i}$	$\sigma_{6,i}$	MAG_AUTO$_i$	$\sigma_{\mathrm{MAG\_AUTO},i}$	Flags
217.5665371 +32.1172020	99.00 18.39 99.00 16.36	99.00 0.13 99.00 0.29	99.00 18.53 99.00 16.74	99.00 0.17 99.00 0.54	99.00 18.73 99.00 17.11	99.00 0.13 99.00 0.37	24
216.1924704 +32.1071896	99.00 17.30 99.00 99.00	99.00 0.05 99.00 99.00	99.00 17.25 99.00 17.04	99.00 0.06 99.00 0.82	99.00 17.35 99.00 99.00	99.00 0.06 99.00 99.00	27
216.2097384 +32.1080726	99.00 18.13 99.00 17.66	99.00 0.13 99.00 2.01	99.00 18.07 99.00 99.00	99.00 0.14 99.00 99.00	99.00 18.35 99.00 99.00	99.00 0.12 99.00 99.00	16

Notes. As Table 7, but implementing selection within the full, four-epoch 4.5 μm SDWFS mosaic.
(This table is available in its entirety in a machine-readable form in the online journal. A portion is shown here for guidance regarding its form and content.)

Table 8
SDWFS Four-Epoch, 5.8 μm-Selected Catalog

R.A., Decl. (J2000)	$m_{4,i}$	$\sigma_{4,i}$	$m_{6,i}$	$\sigma_{6,i}$	MAG_AUTO$_i$	$\sigma_{\mathrm{MAG\_AUTO},i}$	Flags
216.8846970 +32.1580491	17.19 17.00 16.32 16.12	0.02 0.04 0.19 0.33	17.13 16.94 16.17 16.16	0.03 0.05 0.17 0.37	17.11 17.28 16.34 99.00	0.04 0.11 0.32 99.00	0
216.8780169 +32.1638692	18.39 17.82 16.29 16.11	0.07 0.09 0.18 0.33	18.14 17.75 16.05 16.31	0.06 0.10 0.16 0.43	16.99 17.09 15.43 99.00	0.04 0.11 0.16 99.00	0
216.8807521 +32.1636509	16.40 16.23 15.56 14.86	0.01 0.02 0.10 0.11	16.17 16.03 15.26 14.79	0.01 0.02 0.07 0.10	15.58 15.93 14.31 14.97	0.02 0.07 0.10 0.37	0

Notes. As Table 7, but implementing selection within the full, four-epoch 5.8 μm SDWFS mosaic.
(This table is available in its entirety in a machine-readable form in the online journal. A portion is shown here for guidance regarding its form and content.)

Table 9
SDWFS Four-Epoch, 8.0 μm-Selected Catalog

R.A., Decl. (J2000)	$m_{4,i}$	$\sigma_{4,i}$	$m_{6,i}$	$\sigma_{6,i}$	MAG_AUTO$_i$	$\sigma_{\mathrm{MAG\_AUTO},i}$	Flags
216.1899512 +32.1081285	99.00 14.43 99.00 14.24	99.00 0.00 99.00 0.06	99.00 14.42 99.00 14.19	99.00 0.00 99.00 0.06	20.74 14.50 99.00 14.33	2.55 0.01 99.00 0.08	16
217.0852837 +32.1234650	99.00 15.44 99.00 15.39	99.00 0.01 99.00 0.16	99.00 15.38 99.00 15.38	99.00 0.01 99.00 0.18	99.00 15.46 99.00 15.36	99.00 0.02 99.00 0.18	0
216.1933866 +32.1156223	99.00 16.60 99.00 15.48	99.00 0.04 99.00 0.22	99.00 16.01 99.00 15.24	99.00 0.02 99.00 0.15	20.64 15.30 99.00 15.45	1.98 0.02 99.00 0.24	0

Notes. As Table 7, but implementing selection within the full, four-epoch 8.0 μm SDWFS mosaic.
(This table is available in its entirety in a machine-readable form in the online journal. A portion is shown here for guidance regarding its form and content.)

Table 10
SDWFS First-Epoch, 3.6 μm-Selected Catalog

R.A., Decl. (J2000)	$m_{4,i}$	$\sigma_{4,i}$	$m_{6,i}$	$\sigma_{6,i}$	MAG_AUTO$_i$	$\sigma_{\mathrm{MAG\_AUTO},i}$	Flags
218.2410983 +32.3110349	18.80 99.00 99.00 99.00	0.16 99.00 99.00 99.00	18.84 99.00 99.00 99.00	0.21 99.00 99.00 99.00	19.11 99.00 99.00 99.00	0.33 99.00 99.00 99.00	2
218.2296437 +32.3150555	18.61 99.00 99.00 99.00	0.15 99.00 99.00 99.00	18.73 99.00 99.00 99.00	0.19 99.00 99.00 99.00	18.98 99.00 99.00 99.00	0.30 99.00 99.00 99.00	0
218.2327133 +32.3136986	16.93 99.00 99.00 99.00	0.03 99.00 99.00 99.00	16.85 99.00 16.91 99.00	0.03 99.00 0.82 99.00	16.93 99.00 99.00 99.00	0.06 99.00 99.00 99.00	0

Notes. Format as Table 7, but for the first-epoch SDWFS sources, incorporating a selection at 3.6 μm based on the total SDWFS co-add.
(This table is available in its entirety in a machine-readable form in the online journal. A portion is shown here for guidance regarding its form and content.)

Table 11
SDWFS First-Epoch, 4.5 μm-Selected Catalog

R.A., Decl. (J2000)	$m_{4,i}$	$\sigma_{4,i}$	$m_{6,i}$	$\sigma_{6,i}$	MAG_AUTO$_i$	$\sigma_{\mathrm{MAG\_AUTO},i}$	Flags
218.1755258 +32.2135628	99.00 17.71 99.00 15.70	99.00 0.15 99.00 0.40	99.00 17.73 99.00 15.39	99.00 0.19 99.00 0.35	99.00 17.79 99.00 15.55	99.00 0.19 99.00 0.31	0
218.1709414 +32.2140743	99.00 18.16 99.00 16.22	99.00 0.22 99.00 2.21	99.00 18.33 99.00 15.96	99.00 0.33 99.00 0.63	99.00 18.62 99.00 16.84	99.00 0.40 99.00 1.58	3
218.1711818 +32.2155026	99.00 16.54 99.00 99.00	99.00 0.05 99.00 99.00	99.00 16.52 99.00 15.52	99.00 0.06 99.00 0.39	99.00 16.52 99.00 15.50	99.00 0.07 99.00 0.39	2

Notes. Format as Table 7, but for the first-epoch SDWFS sources, incorporating a selection at 4.5 μm based on the total SDWFS co-add.
(This table is available in its entirety in a machine-readable form in the online journal. A portion is shown here for guidance regarding its form and content.)

Table 12
SDWFS First-Epoch, 5.8 μm-Selected Catalog

R.A., Decl. (J2000)	$m_{4,i}$	$\sigma_{4,i}$	$m_{6,i}$	$\sigma_{6,i}$	MAG_AUTO$_i$	$\sigma_{\mathrm{MAG\_AUTO},i}$	Flags
218.2483469 +32.3236056	99.00 99.00 14.69 99.00	99.00 99.00 0.25 99.00	99.00 99.00 12.31 99.00	99.00 99.00 0.01 99.00	99.00 99.00 10.51 99.00	99.00 99.00 0.00 99.00	3
216.3420939 +32.3147357	16.75 16.31 15.65 14.36	0.03 0.04 0.18 0.13	16.50 16.18 15.83 14.25	0.02 0.04 0.26 0.12	16.48 16.23 15.32 14.21	0.04 0.07 0.24 0.15	0
218.2527709 +32.3242584	99.00 99.00 12.59 99.00	99.00 99.00 0.02 99.00	99.00 99.00 12.10 99.00	99.00 99.00 0.01 99.00	99.00 99.00 11.50 99.00	99.00 99.00 0.01 99.00	0

Notes. Format as Table 7, but for the first-epoch SDWFS sources, incorporating a selection at 5.8 μm based on the total SDWFS co-add.
(This table is available in its entirety in a machine-readable form in the online journal. A portion is shown here for guidance regarding its form and content.)

Table 13
SDWFS First-Epoch, 8.0 μm-Selected Catalog

R.A., Decl. (J2000)	$m_{4,i}$	$\sigma_{4,i}$	$m_{6,i}$	$\sigma_{6,i}$	MAG_AUTO$_i$	$\sigma_{\mathrm{MAG\_AUTO},i}$	Flags
216.2963348 +32.2085586	99.00 16.96 99.00 14.43	99.00 0.07 99.00 0.15	99.00 16.75 99.00 14.12	99.00 0.07 99.00 0.10	99.00 17.09 99.00 13.61	99.00 0.25 99.00 0.13	0
218.1546740 +32.2255813	99.00 16.50 99.00 15.00	99.00 0.05 99.00 0.19	99.00 16.45 99.00 15.05	99.00 0.06 99.00 0.25	99.00 16.32 99.00 14.47	99.00 0.08 99.00 0.18	0
218.1497132 +32.2287087	99.00 17.23 99.00 14.78	99.00 0.09 99.00 0.17	99.00 17.24 99.00 14.74	99.00 0.12 99.00 0.18	99.00 17.45 99.00 15.19	99.00 0.17 99.00 0.27	0

Notes. Format as Table 7, but for the first-epoch SDWFS sources, incorporating a selection at 8.0 μm based on the total SDWFS co-add.
(This table is available in its entirety in a machine-readable form in the online journal. A portion is shown here for guidance regarding its form and content.)

Table 14
SDWFS Second-Epoch, 3.6 μm-Selected Catalog

R.A., Decl. (J2000)	$m_{4,i}$	$\sigma_{4,i}$	$m_{6,i}$	$\sigma_{6,i}$	MAG_AUTO$_i$	$\sigma_{\mathrm{MAG\_AUTO},i}$	Flags
216.8795190 +32.1472610	17.45 99.00 99.00 99.00	0.05 99.00 99.00 99.00	17.49 99.00 17.14 99.00	0.06 99.00 1.03 99.00	17.61 99.00 16.03 99.00	0.09 99.00 0.36 99.00	0
216.8779087 +32.1508507	18.95 99.00 16.34 99.00	0.19 99.00 0.57 99.00	19.00 99.00 15.57 99.00	0.24 99.00 0.19 99.00	19.27 99.00 15.32 99.00	0.38 99.00 0.16 99.00	0
216.8690172 +32.1546013	19.11 99.00 16.68 99.00	0.25 99.00 0.76 99.00	18.81 99.00 15.90 99.00	0.20 99.00 0.26 99.00	18.23 99.00 14.44 99.00	0.25 99.00 0.13 99.00	0

Notes. Format as Table 7, but for the second-epoch SDWFS sources, incorporating a selection at 3.6 μm based on the total SDWFS co-add.
(This table is available in its entirety in a machine-readable form in the online journal. A portion is shown here for guidance regarding its form and content.)

Table 15
SDWFS Second-Epoch, 4.5 μm-Selected Catalog

R.A., Decl. (J2000)	$m_{4,i}$	$\sigma_{4,i}$	$m_{6,i}$	$\sigma_{6,i}$	MAG_AUTO$_i$	$\sigma_{\mathrm{MAG\_AUTO},i}$	Flags
216.7849482 +32.1982162	17.94 17.64 16.79 99.00	0.07 0.12 1.72 99.00	17.81 17.64 16.22 16.31	0.08 0.16 0.35 0.95	17.87 17.72 15.97 16.76	0.09 0.19 0.27 2.00	0
216.7747301 +32.2006268	18.61 17.54 16.12 14.63	0.15 0.13 0.30 0.18	18.41 17.40 15.92 14.47	0.14 0.13 0.26 0.14	18.55 17.57 16.12 14.89	0.14 0.14 0.26 0.15	0
216.7836897 +32.2008446	16.56 16.47 16.27 15.30	0.02 0.05 0.37 0.29	16.45 16.43 15.93 15.14	0.02 0.05 0.26 0.26	16.51 16.58 15.60 15.30	0.03 0.08 0.22 0.31	0

Notes. Format as Table 7, but for the second-epoch SDWFS sources, incorporating a selection at 4.5 μm based on the total SDWFS co-add.
(This table is available in its entirety in a machine-readable form in the online journal. A portion is shown here for guidance regarding its form and content.)

Table 16
SDWFS Second-Epoch, 5.8 μm-Selected Catalog

R.A., Decl. (J2000)	$m_{4,i}$	$\sigma_{4,i}$	$m_{6,i}$	$\sigma_{6,i}$	MAG_AUTO$_i$	$\sigma_{\mathrm{MAG\_AUTO},i}$	Flags
216.8796119 +32.1544672	99.00 99.00 15.66 99.00	99.00 99.00 0.22 99.00	99.00 99.00 15.40 99.00	99.00 99.00 0.16 99.00	99.00 99.00 15.12 99.00	99.00 99.00 0.15 99.00	0
216.8846970 +32.1580491	17.24 99.00 15.73 99.00	0.04 99.00 0.23 99.00	17.20 99.00 15.44 99.00	0.05 99.00 0.16 99.00	17.21 99.00 14.89 99.00	0.08 99.00 0.15 99.00	0
216.8807521 +32.1636509	16.43 99.00 15.15 99.00	0.02 99.00 0.14 99.00	16.17 99.00 14.77 99.00	0.02 99.00 0.09 99.00	15.68 99.00 13.34 99.00	0.04 99.00 0.08 99.00	0

Notes. Format as Table 7, but for the second-epoch SDWFS sources, incorporating a selection at 5.8 μm based on the total SDWFS co-add.
(This table is available in its entirety in a machine-readable form in the online journal. A portion is shown here for guidance regarding its form and content.)

Table 17
SDWFS Second-Epoch, 8.0 μm-Selected Catalog

R.A., Decl. (J2000)	$m_{4,i}$	$\sigma_{4,i}$	$m_{6,i}$	$\sigma_{6,i}$	MAG_AUTO$_i$	$\sigma_{\mathrm{MAG\_AUTO},i}$	Flags
216.7747441 +32.2004259	18.67 17.69 16.06 14.57	0.16 0.14 0.28 0.15	18.42 17.47 15.92 14.48	0.14 0.14 0.26 0.14	18.52 17.60 16.16 14.80	0.14 0.14 0.27 0.14	0
216.7681272 +32.2105936	18.14 18.31 99.00 15.10	0.10 0.21 99.00 0.18	18.07 19.11 17.30 15.71	0.10 0.73 1.42 0.46	18.34 99.00 16.76 15.90	0.16 99.00 0.74 0.58	0
216.9966014 +32.2160076	18.12 17.64 16.48 13.88	0.08 0.15 0.40 0.22	18.13 17.55 16.44 12.24	0.11 0.15 0.44 0.02	18.26 17.77 16.61 12.33	0.12 0.18 0.46 0.02	0

Notes. Format as Table 7, but for the second-epoch SDWFS sources, incorporating a selection at 8.0 μm based on the total SDWFS co-add.
(This table is available in its entirety in a machine-readable form in the online journal. A portion is shown here for guidance regarding its form and content.)

Table 18
SDWFS Third-Epoch, 3.6 μm-Selected Catalog

R.A., Decl. (J2000)	$m_{4,i}$	$\sigma_{4,i}$	$m_{6,i}$	$\sigma_{6,i}$	MAG_AUTO$_i$	$\sigma_{\mathrm{MAG\_AUTO},i}$	Flags
217.2022991 +32.2039361	18.48 99.00 99.00 16.38	0.15 99.00 99.00 0.84	18.06 99.00 99.00 99.00	0.10 99.00 99.00 99.00	17.92 99.00 99.00 99.00	0.10 99.00 99.00 99.00	0
217.2056241 +32.2072504	18.30 99.00 99.00 99.00	0.11 99.00 99.00 99.00	18.07 99.00 99.00 16.23	0.11 99.00 99.00 0.96	18.16 99.00 99.00 16.22	0.12 99.00 99.00 0.71	1
217.2033917 +32.2074459	17.99 18.39 99.00 15.03	0.09 0.34 99.00 0.28	17.73 18.27 99.00 14.68	0.08 0.33 99.00 0.18	17.45 99.00 16.78 15.13	0.09 99.00 1.27 0.37	0

Notes. Format as Table 7, but for the third-epoch SDWFS sources, incorporating a selection at 3.6 μm based on the total SDWFS co-add.
(This table is available in its entirety in a machine-readable form in the online journal. A portion is shown here for guidance regarding its form and content.)

Table 19
SDWFS Third-Epoch, 4.5 μm-Selected Catalog

R.A., Decl. (J2000)	$m_{4,i}$	$\sigma_{4,i}$	$m_{6,i}$	$\sigma_{6,i}$	MAG_AUTO$_i$	$\sigma_{\mathrm{MAG\_AUTO},i}$	Flags
218.0399336 +32.1355066	99.00 17.71 99.00 99.00	99.00 0.17 99.00 99.00	99.00 17.64 99.00 99.00	99.00 0.18 99.00 99.00	99.00 17.71 99.00 99.00	99.00 0.20 99.00 99.00	0
217.0086076 +32.1368397	99.00 16.70 99.00 16.17	99.00 0.08 99.00 2.30	99.00 16.34 99.00 15.54	99.00 0.05 99.00 0.42	99.00 16.40 99.00 15.13	99.00 0.09 99.00 0.36	0
218.0409377 +32.1412184	99.00 17.85 99.00 99.00	99.00 0.19 99.00 99.00	99.00 17.84 99.00 99.00	99.00 0.22 99.00 99.00	99.00 17.98 99.00 99.00	99.00 0.23 99.00 99.00	0

Notes. Format as Table 7, but for the third-epoch SDWFS sources, incorporating a selection at 4.5 μm based on the total SDWFS co-add.
(This table is available in its entirety in a machine-readable form in the online journal. A portion is shown here for guidance regarding its form and content.)

Table 20
SDWFS Third-Epoch, 5.8 μm-Selected Catalog

R.A., Decl. (J2000)	$m_{4,i}$	$\sigma_{4,i}$	$m_{6,i}$	$\sigma_{6,i}$	MAG_AUTO$_i$	$\sigma_{\mathrm{MAG\_AUTO},i}$	Flags
217.1870834 +32.2105374	99.00 17.63 15.74 16.34	99.00 0.17 0.24 1.19	99.00 17.45 15.49 16.31	99.00 0.15 0.18 1.08	17.99 17.54 12.52 14.43	0.23 0.39 0.03 0.28	0
216.9497752 +32.2168119	15.91 15.86 15.59 15.50	0.01 0.03 0.20 0.40	15.65 15.64 15.50 15.18	0.01 0.03 0.19 0.29	15.41 15.43 16.21 14.50	0.02 0.06 1.27 0.35	3
217.1808066 +32.2194348	15.45 15.73 15.72 15.14	0.01 0.02 0.25 0.26	15.41 15.71 15.42 15.13	0.01 0.03 0.17 0.28	14.98 16.72 15.03 13.53	0.02 0.26 0.38 0.17	0

Notes. Format as Table 7, but for the third-epoch SDWFS sources, incorporating a selection at 5.8 μm based on the total SDWFS co-add.
(This table is available in its entirety in a machine-readable form in the online journal. A portion is shown here for guidance regarding its form and content.)

Table 21
SDWFS Third-Epoch, 8.0 μm-Selected Catalog

R.A., Decl. (J2000)	$m_{4,i}$	$\sigma_{4,i}$	$m_{6,i}$	$\sigma_{6,i}$	MAG_AUTO$_i$	$\sigma_{\mathrm{MAG\_AUTO},i}$	Flags
218.0345373 +32.1436154	99.00 16.06 99.00 14.91	99.00 0.04 99.00 0.21	99.00 16.07 99.00 14.88	99.00 0.04 99.00 0.22	99.00 16.24 99.00 15.06	99.00 0.06 99.00 0.24	0
216.6480548 +32.1409453	99.00 99.00 99.00 13.04	99.00 99.00 99.00 0.04	99.00 99.00 99.00 13.12	99.00 99.00 99.00 0.04	99.00 99.00 99.00 13.50	99.00 99.00 99.00 0.07	0
218.0494313 +32.1458605	99.00 15.71 99.00 13.33	99.00 0.03 99.00 0.05	99.00 15.64 99.00 13.27	99.00 0.03 99.00 0.05	99.00 15.72 99.00 13.40	99.00 0.04 99.00 0.07	0

Notes. Format as Table 7, but for the third-epoch SDWFS sources, incorporating a selection at 8.0 μm based on the total SDWFS co-add.
(This table is available in its entirety in a machine-readable form in the online journal. A portion is shown here for guidance regarding its form and content.)

Table 22
SDWFS Fourth-Epoch, 3.6 μm-Selected Catalog

R.A., Decl. (J2000)	$m_{4,i}$	$\sigma_{4,i}$	$m_{6,i}$	$\sigma_{6,i}$	MAG_AUTO$_i$	$\sigma_{\mathrm{MAG\_AUTO},i}$	Flags
216.3064840 +32.1872639	18.25 17.71 16.13 16.45	0.11 0.16 0.29 0.85	18.07 17.49 16.11 16.34	0.10 0.14 0.30 0.98	18.20 17.61 16.40 16.54	0.10 0.14 0.32 0.78	3
216.7761606 +32.1925195	18.59 19.23 16.54 99.00	0.14 0.71 0.44 99.00	18.41 19.05 16.20 99.00	0.14 0.69 0.33 99.00	18.11 19.37 16.42 99.00	0.13 2.55 0.50 99.00	2
216.7971180 +32.1938184	18.46 19.03 99.00 16.21	0.14 0.49 99.00 2.01	18.04 18.84 99.00 15.11	0.10 0.54 99.00 0.25	17.50 18.72 99.00 14.42	0.08 0.69 99.00 0.15	2

Notes. Format as Table 7, but for the fourth-epoch SDWFS sources, incorporating a selection at 3.6 μm based on the total SDWFS co-add.
(This table is available in its entirety in a machine-readable form in the online journal. A portion is shown here for guidance regarding its form and content.)

Table 23
SDWFS Fourth-Epoch, 4.5 μm-Selected Catalog

R.A., Decl. (J2000)	$m_{4,i}$	$\sigma_{4,i}$	$m_{6,i}$	$\sigma_{6,i}$	MAG_AUTO$_i$	$\sigma_{\mathrm{MAG\_AUTO},i}$	Flags
217.3516233 +32.1541013	99.00 17.30 99.00 16.17	99.00 0.10 99.00 0.69	99.00 17.46 99.00 15.87	99.00 0.14 99.00 0.54	99.00 17.80 99.00 16.19	99.00 0.21 99.00 0.67	0
217.8643815 +32.1544045	99.00 17.08 99.00 15.86	99.00 0.07 99.00 0.98	99.00 17.18 99.00 15.85	99.00 0.11 99.00 0.53	99.00 17.32 99.00 15.59	99.00 0.14 99.00 0.38	3
217.8627125 +32.1547360	99.00 15.71 99.00 14.80	99.00 0.02 99.00 0.20	99.00 15.56 99.00 14.46	99.00 0.02 99.00 0.14	99.00 15.44 99.00 14.52	99.00 0.03 99.00 0.18	3

Notes. Format as Table 7, but for the fourth-epoch SDWFS sources, incorporating a selection at 4.5 μm based on the total SDWFS co-add.
(This table is available in its entirety in a machine-readable form in the online journal. A portion is shown here for guidance regarding its form and content.)

Table 24
SDWFS Fourth-Epoch, 5.8 μm-Selected Catalog

R.A., Decl. (J2000)	$m_{4,i}$	$\sigma_{4,i}$	$m_{6,i}$	$\sigma_{6,i}$	MAG_AUTO$_i$	$\sigma_{\mathrm{MAG\_AUTO},i}$	Flags
216.3143103 +32.1907240	16.56 16.31 15.76 15.65	0.02 0.04 0.23 0.41	16.40 16.14 15.47 15.50	0.02 0.04 0.16 0.37	15.93 15.73 15.39 99.00	0.04 0.09 0.46 99.00	2
216.7530185 +32.1992019	14.75 14.96 15.00 14.97	0.00 0.01 0.11 0.20	14.71 14.91 14.82 15.01	0.00 0.01 0.09 0.23	14.60 14.72 14.71 15.29	0.01 0.02 0.15 0.52	0
216.2371374 +32.1955547	15.49 15.03 14.66 12.75	0.01 0.01 0.08 0.03	15.33 14.91 14.46 12.68	0.01 0.01 0.06 0.03	15.02 14.66 13.83 12.49	0.02 0.04 0.13 0.07	2

Notes. Format as Table 7, but for the fourth-epoch SDWFS sources, incorporating a selection at 5.8 μm based on the total SDWFS co-add.
(This table is available in its entirety in a machine-readable form in the online journal. A portion is shown here for guidance regarding its form and content.)

Table 25
SDWFS Fourth-Epoch, 8.0 μm-Selected Catalog

R.A., Decl. (J2000)	$m_{4,i}$	$\sigma_{4,i}$	$m_{6,i}$	$\sigma_{6,i}$	MAG_AUTO$_i$	$\sigma_{\mathrm{MAG\_AUTO},i}$	Flags
217.8626725 +32.1545472	99.00 15.76 99.00 14.75	99.00 0.03 99.00 0.19	99.00 15.60 99.00 14.40	99.00 0.03 99.00 0.13	99.00 15.76 99.00 14.75	99.00 0.02 99.00 0.12	0
217.3706421 +32.1574812	99.00 15.01 99.00 14.49	99.00 0.01 99.00 0.13	99.00 15.01 99.00 14.40	99.00 0.01 99.00 0.13	99.00 15.09 99.00 13.94	99.00 0.02 99.00 0.11	0
217.3174334 +32.1592254	99.00 99.00 99.00 14.86	99.00 99.00 99.00 0.19	99.00 18.62 99.00 14.82	99.00 0.42 99.00 0.19	99.00 18.99 99.00 15.32	99.00 0.44 99.00 0.18	0

Notes. Format as Table 7, but for the fourth-epoch SDWFS sources, incorporating a selection at 8.0 μm based on the total SDWFS co-add.
(This table is available in its entirety in a machine-readable form in the online journal. A portion is shown here for guidance regarding its form and content.)

area density, i.e., the source counts. Accordingly, we plot the differential SDWFS number counts in Figure 12. The panels illustrate total counts (stars plus galaxies) in all four IRAC bands. For comparison, the stellar counts from Fazio et al. (2004) are also shown. Stars dominate the counts at the bright end of the distribution, but at the faint end, the counts are dominated by galaxies.

Figure 12 also compares the SDWFS count distribution to that of Fazio et al. (2004). The latter are drawn from the original ISS and constitute the first SDWFS epoch. The agreement is excellent throughout, although the deeper SDWFS data permit the counts to be estimated to fainter levels than was originally possible for this field. Both sets of counts exhibit a change in slope at $[3.6] \approx 17$, consistent with what is seen in other work (e.g., Sullivan et al. 2007). The point of inflection seen in the 3.6 μm counts is consistent with the models of Gardner (1998), which extrapolate K-band counts into the IRAC 3.6 μm band. Essentially, the negative K-correction of a passively evolving population formed at high redshift ($z \gtrsim 3$) produces a roughly constant apparent magnitude in the shorter-wavelength IRAC bands for $0.7 \lesssim z \lesssim 2$ (see Figure 1 of Eisenhardt et al. 2008).

At the faint end, the SDWFS counts are in excellent agreement with those drawn from the much deeper IRAC survey of the EGS (Barmby et al. 2008). The differences appear when the counts approach the 5σ limit, where the SDWFS incompleteness corrections become large and less certain.

4.3. IRAC Color Distribution

For galaxy populations detected in wide-area, relatively shallow surveys like SDWFS, a limited number of emission processes dominate the IRAC SEDs. These include stellar thermal emission from bulge and/or disk populations, to which the 3.6 and 4.5 μm bands are most sensitive. There is also typically a contribution of 7.7 μm polycyclic aromatic hydrocarbon (PAH) emission, mostly from low-redshift galaxy disks, as well as the predominantly red emission from AGN that often takes the form of a power law. These contributions to the IRAC SEDs are reflected in the way SDWFS sources are distributed in the IRAC color–color space shown in Figure 13. Broadly speaking, their distribution is consistent with that shown in other surveys. A number of sources fall near the origin in this color–color space; these are the stars and low-redshift galaxies dominated by starlight (e.g., elliptical galaxies). Indeed, the colors of elliptical galaxy NGC 4429 intersect this locus of points at modest redshift. Sources that are red in $[5.8] - [8.0]$ and relatively blue at shorter wavelengths ($[3.6] - [4.5] < 0.5$) are consistent with emission from nearby galaxies rapidly forming stars. Objects like these generate significant 7.7 μm PAH emission and therefore appear red to IRAC. The $0 \leqslant z \leqslant 2$ non-evolutionary track shown for M 82 in this color–color space follows the distribution of these sources remarkably well.

Finally, the portion of Figure 13 enclosed within the dotted line (the "Stern wedge", Stern et al. 2005; see also Lacy et al. 2004) is a regime that by construction contains galaxies that are red in both $[5.8] - [8.0]$ and $[3.6] - [4.5]$. At redshifts below 1.5, objects that lie in this region of color–color space have mid-IR SEDs that are closely approximated by a power law and are predominantly AGN. A large fraction of the X-ray-detected sources in Boötes lie in this region (Gorjian et al. 2008). While it is true that high-redshift, star-forming galaxies ($z > 2$) can enter the Stern et al. AGN region (e.g., Stern et al. 2005; Barmby et al. 2008), such objects generally have 5.8 and 8.0 μm fluxes that fall below the SDWFS flux limits, so they are thought not to be a significant contaminant at SDWFS depths.

4.4. Mid-Infrared Detections of Radio Sources

The Faint Images of the Radio Sky at Twenty cm (FIRST; Becker et al. 1995) survey mapped 9055 deg^2 of the north and south Galactic caps with the VLA, reaching a typical 5σ detection threshold of 0.75 mJy at 1.4 GHz. This large survey, which includes the Boötes field, has a source density of $\sim$90 sources deg^{-2} and a typical positional accuracy of 1″. Approximately 30% of the sources have optical identifications in the Sloan Digital Sky Survey (SDSS; Ivezić et al. 2002). Here, we consider the IRAC properties of FIRST sources as observed by SDWFS.

According to the latest catalog (2008 October 31), 887 FIRST sources fall in the 3.6 μm SDWFS coverage map. While several techniques have been presented in the literature for cross-correlating radio catalogs with catalogs at shorter wavelength, Sullivan et al. (2004) demonstrated that positional coincidence is sufficient when both the radio and shorter-wavelength catalogs have high positional accuracies. We therefore adopted a simple, empirically derived 2″ match radius to identify IRAC counterparts to FIRST sources. An identical match radius was used by El Bouchefry & Cress (2007) when matching FIRST to the NDWFS optical and near-IR Boötes data. Given the source density of 5σ IRAC sources from the stacked SDWFS data set, this match radius will yield a 7.3% spurious identification rate at the 5σ limit of the 3.6 μm images (4″-diameter apertures), falling to 1.0% at 8.0 μm. The spurious match rate will, of course, be smaller for brighter sources. We find 3.6 μm identifications for 570 (64.3%) of the FIRST sources. However, approximately 30% of FIRST sources have resolved structure on scales of 2–30″, with the classic example being a double-lobed radio source comprised of two radio-emitting lobes separated by several arcseconds straddling a host galaxy. Our simple position matching scheme will yield no (correct) identifications for such a configuration. We have attempted to minimize the number of such systems by considering only isolated FIRST sources, defined to be at least 30″ from the next nearest FIRST source. The average FIRST source density implies only a 2% chance that a FIRST source will have a random, unrelated source within that radius. Of the 887 FIRST sources in SDWFS, 667 are thus defined as isolated, of which 512 (76.8%) have IRAC 3.6 μm identifications. Figure 14 shows how this identification rate depends both on IRAC passband and mid-IR survey depth for the isolated FIRST sources. Compared to the original ISS, the deeper SDWFS data provide a modest improvement for the 3.6 and 4.5 μm identification fractions but approximately double the number of 5.8 and 8.0 μm identifications. The resulting identification fraction ($> 50\%$) allows us to probe the IRAC color–color distribution of radio sources with higher fidelity (Figure 15). El Bouchefry & Cress (2007) matched 5 deg^2 of the Boötes NDWFS field with the FIRST catalog and found near-infrared identifications for only 40% of FIRST sources (to $K \sim 19.4$) and optical identifications for $\sim$72% of FIRST sources (to B_W, R, $I \sim 25.5$). Approximately 30% of the FIRST sources with robust, four-band SDWFS IRAC identifications have colors consistent with AGN, while the remainder predominantly have colors consistent with galaxies at redshifts above a few tenths.

Tasse et al. (2008a, 2008b) have studied radio source properties on the basis of *XMM-Newton*, the Canada France Hawaii Telescope Legacy Survey (CFHTLS), *Spitzer*, and radio

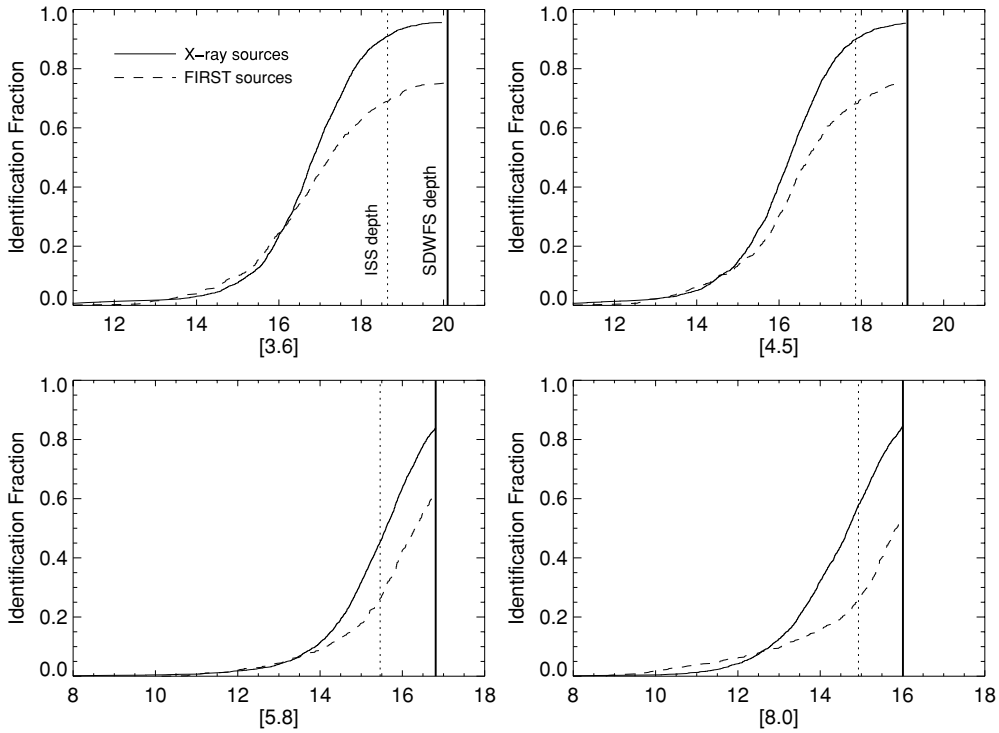

Figure 14. Identification fraction of on-axis X-ray sources (solid curve; $S_{0.5-7\,\mathrm{keV}} \gtrsim 8 \times 10^{-15}\,\mathrm{erg\,cm^{-2}\,s^{-1}}$) and isolated radio sources from the FIRST survey (dashed curve; $S_{1.4\,\mathrm{GHz}} \geqslant 0.75$ mJy) in the Boötes field for all four IRAC bands. The vertical dotted lines show the 5σ depth of the original IRAC Shallow Survey (Eisenhardt et al. 2004). The vertical solid lines show the 5σ depth of SDWFS. The dotted curves show the spurious identification rate as a function of magnitude for $2''$ and $3''$ match radii.

surveys in the *XMM*-LSS field. The radio surveys were carried out with the VLA at 74 and 325 MHz, and with the Giant Meterwave Radio Telescope (GMRT) at 230 and 610 MHz. Tasse et al. found two classes of radio galaxies. The first class consists of massive galaxies that show no signs of infrared excess due to a dusty torus. These galaxies are preferentially found in cluster environments. The second class consists of radio galaxies with less massive hosts. These galaxies do show infrared torus emission and are located in large-scale underdensities. These results are interpreted as being due to AGN that are fed via two different types of accretion. In this scheme, one mode (the "quasar mode") is radiatively efficient and arises from accretion of cold gas onto a supermassive black hole. The other mode (the "radio mode") is radiatively inefficient and results from accretion of hot gas onto a supermassive black hole. Quasar-mode objects are predominantly located inside the Stern et al. (2005) wedge, but radio-mode objects lie outside it.

Deeper (but lower spatial resolution) 1.4 GHz observations of approximately 7 deg^2 of the Boötes field were presented by de Vries et al. (2002). These data, obtained with the Westerbork Synthesis Radio Telescope, reach a 5σ sensitivity of 140 μJy, approximately five times the depth of the FIRST survey, and detect 3172 distinct sources. At the $13''\times27''$ resolution of the Westerbork beam, 316 sources are spatially resolved. We consider only the 2856 unresolved radio sources. The coarse spatial resolution of this survey implies that a larger match radius should be used than was used for FIRST. However, the SDWFS data are sufficiently sensitive that a larger match radius will yield a prohibitively large number of spurious identifications. We instead opt for a $2''$ positional match radius where reliability should be high but completeness will be compromised. The 1392 (48.7%) IRAC counterparts thus conservatively identified are a poor probe of the mid-IR identification rate for faint radio sources. They probe the mid-IR colors of radio sources below the FIRST limit (Figure 15). As expected (e.g., Seymour et al. 2008) at these fainter radio fluxes, we see a large population of star-forming galaxies as shown by their red [5.8] − [8.0] colors due to PAH emission in the reddest IRAC bandpass.

4.5. Mid-Infrared Detections of X-ray Sources

The XBoötes survey (Murray et al. 2005; Brand et al. 2006) imaged roughly 8.5 deg^2 in Boötes to a depth of 5 ks using the Advanced CCD Imaging Spectrometer (ACIS) on the *Chandra X-Ray Observatory*. This survey, which consisted of 126 separate, contiguous ACIS observations, identified 3293 sources detected with four or more counts in the full 0.5–7 keV band (Kenter et al. 2005), corresponding to a flux of $7.8 \times 10^{-15}\,\mathrm{erg\,cm^{-2}\,s^{-1}}$ for on-axis sources. The spurious detection rate was approximately 1%. The spatial resolution of *Chandra* degrades quadratically with off-axis distance, ranging from only $0\farcs6$ (FWHM) on-axis to $6\farcs0$ when $10'$ off-axis. We considered the 2243 (68.1%) of XBoötes sources with positional uncertainties $\leqslant 2''$ and performed a simple position match within a $3''$ match radius. This match radius will yield a 16.4% spurious identification rate at the 5σ limit of the 3.6 μm data ($4''$-diameter aperture), falling to 2.3% at 8.0 μm, assuming that IRAC sources are randomly distributed. The spurious identification rate, of course, is lower for brighter mid-IR sources. After applying a small, empirically derived shift to the X-ray astrometric frame (ΔR.A. $= -0\farcs335$, Δdecl. $= +0\farcs467$), we find IRAC 3.6 μm identifications for 96.9% of the subsample

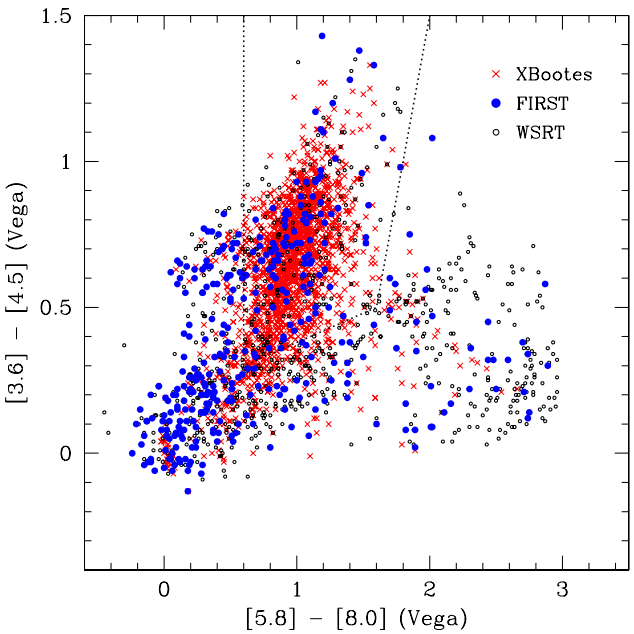

Figure 15. IRAC color–color plot for X-ray sources (red crosses) and radio sources (filled blue circles and open circles) detected in all four IRAC bands. The open circles show 1.4 GHz sources fainter than the FIRST 0.75 mJy limit identified from deeper Westerbork Synthesis Radio Telescope (WSRT) observations (de Vries et al. 2002). The dotted lines indicate the (Stern et al. 2005) AGN wedge.

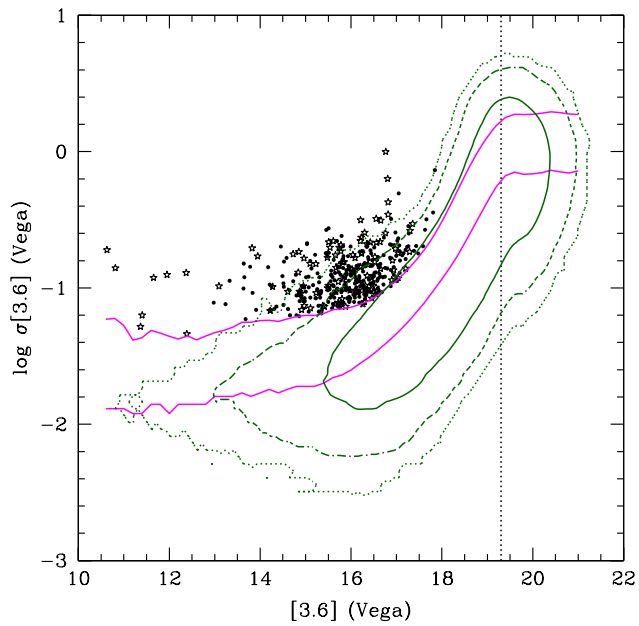

Figure 16. Distribution of $\sim$440, 000 SDWFS sources in magnitude-log(σ) space, where σ represents the variation in photometry over four epochs at 3.6 μm. The sources were binned at 0.1 mag intervals, and within these bins, both the median photometric variation ($\bar{\sigma}$) and the dispersion with respect to that median ($\hat{\sigma}$) were computed. The green contours show the magnitude-log(σ) distribution of SDWFS sources when binned in 0.1 mag intervals and 0.05 log(σ) bins, indicating 2, 10, and 100 sources per bin. The median variation $\bar{\sigma}$ and the 1.5 $\hat{\sigma}$ level of significance above $\bar{\sigma}$ are indicated by the lower and upper magenta lines, respectively. A total of 379 objects satisfy the variability criteria described in the text, i.e., $\sigma > 1.5\hat{\sigma} + \bar{\sigma}$. Sources that lie within (outside) the AGN wedge are indicated with filled circles (open stars). The vertical dotted line at [3.6] = 19.3 mag marks the limiting magnitude of the variability study.

of unresolved XBoötes sources with small positional accuracies; 80.0% have robust, four-band IRAC identifications. Thus, while the generous match radius would suggest a large number of spurious 3.6 μm identifications, the $>$ 80% match rate at 8.0 μm suggests that few of the shorter-wavelength identifications are, in fact, incorrect. Visual inspection shows that only $\sim$1% of the X-ray sources correspond to blank fields at 3.6 μm, roughly consistent with the expected spurious rate for the four-count catalog. Figure 14 shows how the XBoötes identification rate depends both on IRAC passband and mid-IR survey depth. Relative to the original ISS, the deeper SDWFS data nearly double the number of X-ray sources with robust, four-band IRAC detections.

Figure 15 shows the IRAC color–color properties of XBoötes sources. Similar to the results of Gorjian et al. (2008), which matched XBoötes to the original ISS, 77.1% of the X-ray sources satisfy the color-selection criteria developed by Stern et al. (2005) to select active galaxies in the mid-IR. For comparison, Gorjian et al. (2008) found robust, four-band IRAC identifications for only 42.9% of the XBoötes sources in the shallower ISS data, of which 65.2% have AGN-like IRAC colors. If we restrict a similar analysis to XBoötes sources with $\leqslant 2''$ positional accuracies at the single-epoch 5σ depths, 61.0% have robust, four-band IRAC identifications, of which 80.0% satisfy the IRAC AGN selection criteria of Stern et al. (2005). In brief, then, the deeper SDWFS data significantly increase the number of X-ray sources with robust, four-band photometry. However, the nature of the identified sources does not appear to change significantly, with approximately 80% of the well-characterized X-ray sources still having mid-IR colors indicative of AGN activity dominating at IRAC wavelengths. As shown by Hickox et al. (2007), stacking the X-ray data for IRAC-selected AGN candidates lacking direct detections in the XBoötes data show that such sources, on average, harbor high-luminosity, obscured AGN.

4.6. Infrared-Variable Sources

We have analyzed the four SDWFS epochs to perform a blind search for infrared-variable sources using difference imaging (e.g., Alard & Lupton 1998; Woźniak 2000). Details and complete results will be reported elsewhere (S. Kozłowski et al. 2009, in preparation) but we present initial findings here. Each single-epoch mosaic was prepared for difference imaging by constructing a smoothed estimate of the *Spitzer* PSF. We used Fourier methods to create new versions of the mosaics in which the native IRAC PSFs were converted into Gaussians of similar width. This removed the complex, rotated diffraction spikes for which difference imaging algorithms are not generally designed. We then used the Difference Image Analysis package (DIA; Woźniak 2000) to subtract successive SDWFS epochs.

The variability (dispersion) was estimated for each object detected in the four difference images, where the average image of the four epochs was subtracted from each epoch. The difference imaging techniques were very useful in the data processing phase discussed in Section 2.2 because they allowed rapid identification of artifacts in the SDWFS mosaics. With almost all the sources vanishing (because they are not variable), even low level artifacts stood out. More importantly, this technique directly addresses the greatest limitation of mid-IR color selection of AGN: that it begins to fail as the AGN luminosities approach those of the host galaxies and the combined mid-IR colors become bluer (Figure 13). This makes it difficult to identify lower-redshift, lower-luminosity AGN. Difference imaging eliminates the contaminating hosts and extend the detectability of AGN in the mid-IR into the host-

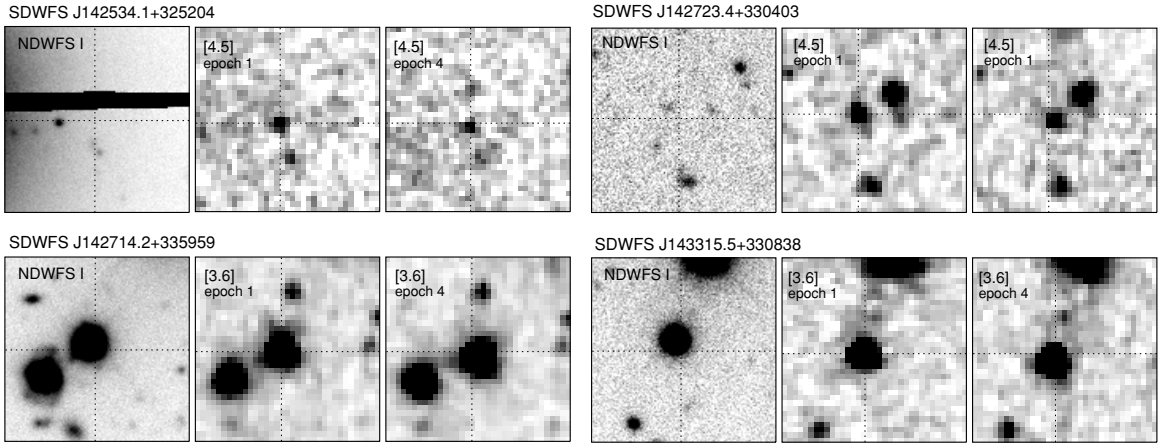

Figure 17. Images of the four sources with the highest measured proper motions across the four-epoch SDWFS campaign. The left image of each triple shows the NDWFS *I*-band image (circa 2000), the center image shows the first-epoch SDWFS image (2004 January), and the right image shows the fourth-epoch SDWFS image (2008 March). Images are all 30″ on a side, with north up and east to the left. The cross hairs are centered on the 2004 January position. Two of the sources have colors consistent with mid-T brown dwarfs. The two brightest sources were identified as high proper motion sources at both 3.6 and 4.5 μm. The two fainter, mid-T candidates were only identified as high proper motion candidates in the 4.5 μm mosaics, in which they have higher signal-to-noise ratio.

dominated regime where many X-ray and radio sources are also observed.

The overall dependence of variability on magnitude is shown in Figure 16. Candidate variable sources were selected as significant outliers from the general trend, and, unsurprisingly, the resulting sample is dominated by AGN with a distribution in mid-IR color–color space similar to the X-ray sources of Figure 15. We calculated the dispersions separately at 3.6 and 4.5 μm, as well as the correlations in the changes between the two bands. We designated an object as IR variable if it changed by $\geqslant 1.5\sigma$ in both bands, if those changes were in synchrony (correlation > 0.5), and if the uncertainties in the 3.6 and 4.5 μm magnitudes were below 0.05 mag. We identified 379 variable objects on the basis of these criteria, or about 45 deg^{-2} to the depth of a single SDWFS epoch. Of these, 272 objects were found to reside in the AGN wedge and 107 objects fell outside it (Figure 16).

4.7. High Proper Motion Sources

Of the wide-area surveys done by *Spitzer* to date, SDWFS is unique in its ability to identify high proper motion mid-IR sources. This is particularly promising for identifying the coolest brown dwarfs, because such sources are very faint optically but bright in the mid-IR. For example, mid-T brown dwarfs have $r - [3.6] \approx 10$ (Strauss et al. 1999; Tsvetanov et al. 2000; Patten et al. 2006), implying that the single-epoch SDWFS mosaics reach the equivalent of $r \approx 29$ for the coolest substellar sources. Thus, although SDWFS covers only a small fraction of the sky, it samples $\approx$ 250 times the volume of the full-sky proper-motion catalog of Luyten (1979) for mid-T brown dwarfs. Any cool brown dwarfs identified in a shallow, wide-area survey such as SDWFS would be relatively nearby and thus might be identifiable from their high proper motions alone. In particular, the abundances and mid-IR properties of the coldest brown dwarfs (the so-called *Y dwarfs*) are uncertain (or, at least, untested) currently, providing additional strong motivation for high proper motion mid-IR searches within the SDWFS survey. Since cool brown dwarfs have red $[3.6] - [4.5]$ colors, we searched for high proper motion objects independently in the two bluest IRAC bands.

We began with the SExtractor catalogs for the four single-epoch IRAC images at both 3.6 and 4.5 μm. Each epoch contains approximately 500,000 identified sources, and we cross-matched the catalogs using `mergecats`, a routine from the `imcat` toolkit written by N. Kaiser for rapid positional cross-correlations of large data sets. We matched the first-epoch SDWFS catalog (e.g., our reprocessed original ISS) to both the third and fourth epochs of SDWFS using a 10″ search radius. These last two SDWFS epochs were obtained approximately 1 month apart in Spring 2008, a little more than 4 yr after the first epoch (UT 2004 January 10–14). We then selected objects which moved by at least 1″.25 ($\approx 3.5\sigma$) between both epochs one and three, *and* between epochs one and four. Because epochs three and four were only a month apart (Table 1), this removed many spurious sources with negligible impact on the highest proper motion sources. Epoch two was ignored for this preliminary investigation of high proper motion SDWFS sources. To remove additional spurious sources (e.g., cosmic rays), we also required that the candidates were not saturated and that they varied by less than 0.2 mag between 2004 and 2008. For the 3.6 μm selection, we required that sources were brighter than 18.5 mag in epoch one (aperture-corrected 3″-diameter magnitude). The corresponding requirement for the 4.5 μm selection was $[4.5] \leqslant 18.0$. Although these requirements are somewhat conservative, they should identify the most reliable, highest proper motion sources across the SDWFS data set. Other techniques, such as image subtraction and creating local reference frames, should identify objects with substantially smaller proper motions.

The criteria above led to samples of 27 3.6 μm-selected candidates and 60 4.5 μm-selected candidates. We visually inspected all candidates. Most proved spurious, with the primary contaminant being merged, confused sources. A few others were artifacts from cosmic rays, the stellar bleed trails of bright stars, and sources near the edge of the IRAC mosaics that survived the automated culling. After inspection, four sources survived, with the two brightest identified independently at both 3.6 and 4.5 μm and two fainter sources only identified at 4.5 μm. Of the two single-band candidates, one omission (SDWFS J142534.1+325204) is attributable to a stellar bleed trail affecting the source in the third-epoch 3.6 μm data. The other source, SDWFS J142723.4+330403, had 3.6 μm motions just below our selection thresholds. Because this source has very red $[3.6] - [4.5]$ colors, the 4.5 μm data actually provide

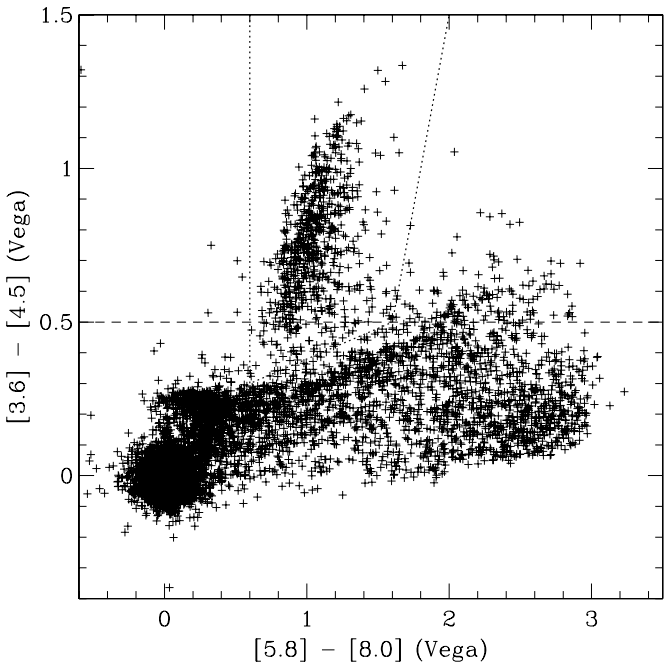

Figure 18. Colors of SDWFS sources that lie above the expected 5σ detection limits of the planned *WISE* all-sky survey. The majority of sources redder than $[3.6] - [4.5] = 0.5$ have the colors of AGN.

higher signal to noise, and we consider this source robustly identified. Table 26 presents the basic information for all four candidates, and Figure 17 presents their *I* band and multi-epoch IRAC images.

The two brightest proper-motion sources are also very bright at visible wavelengths and have $[3.6] - [4.5] \approx 0$, consistent with the Rayleigh–Jeans falloff of main-sequence stars. This inference appears to be borne out in the literature. One of these bright objects, J143315.5+330838, is listed in version 2.3.2 of the Guide Star Catalog as having $\mu(\mathrm{R.A.}) = -70 \pm 3$ mas yr^{-1} and $\mu(\mathrm{decl.}) = -324 \pm 1$ mas yr^{-1} (Lasker et al. 2008), reassuringly consistent with our proper-motion measurements (Table 6). On the basis of its SDSS spectrum, West et al. (2008) assign this object a spectral type of M5—again consistent with the type inferred on the basis of the IRAC color. The other bright IRAC high proper motion source, J142714.2+335959, has a SDWFS proper-motion of $\mu(\mathrm{R.A.}) = -310$ mas yr^{-1} and $\mu(\mathrm{decl.}) = -210$ mas yr^{-1}. This is quite close to the measured values of $\mu(\mathrm{R.A.}) = -288 \pm 3$ mas yr^{-1} and $\mu(\mathrm{decl.}) = -210 \pm 2$ mas yr^{-1} given by Lépine & Shara (2005; the LPSM-NORTH catalog). The SDSS colors of this object appear consistent with it being of spectral type M0 or perhaps M1 (Bochanski et al. 2007).

By contrast, the two fainter SDWFS sources are very faint optically and have red colors across the first two IRAC bands. Their colors ($[3.6] - [4.5] > 0.5$) imply mid-T brown dwarf spectral types (Patten et al. 2006). In particular, SDWFS J142723.4+330403 has $[3.6] - [4.5] = 1.33$, implying a spectral type of approximately T7. P. R. Eisenhardt et al. (2009, in preparation) reported on color-selected brown dwarf candidates with $[3.6] - [4.5] > 1.5$, implying spectral types later than T7. Based on estimated spectral types, the high proper motion sources are at ≈ 100 pc, and have space velocities of order 150 km s^{-1} relative to the Sun.

4.8. SDWFS at the Depth of WISE

The *Wide-field Infrared Survey Explorer* (*WISE*) is scheduled to launch in 2009 November. *WISE* will survey the full sky with a cryogenically cooled 40 cm telescope in four passbands at 3.3, 4.7, 12, and 23 μm. The two shortest *WISE* passbands are similar to the two shortest IRAC passbands. *WISE* will reach 5σ point-source depths of 120 and 160 μJy at 3.3 and 4.7 μm, respectively.

Figure 18 shows the colors of SDWFS sources that would be detected by *WISE* above $[3.6] = 15.91$ and $[4.5] = 15.12$ mag. At these depths, SDWFS identifies 11,910 non-saturated sources with robust, two-band detections. Because *WISE* does not have equivalents of the IRAC 5.8 and 8.0 μm detectors, one might expect that *WISE* will be challenged to separate AGN from galaxies using mid-IR color criteria alone. However, as is clear from Figure 18, at the shallow depth of the planned *WISE* survey, the $[5.8] - [8.0]$ color is unnecessary: nearly every source redder than $[3.6] - [4.5] = 0.5$ is an AGN. The handful of sources to the right of the AGN wedge that lie above this simple color cut are presumably star-forming galaxies at redshifts of a few tenths with dust emission producing their red IRAC colors. Such sources are easily discriminated based on their optical properties.

Based on the 4″-diameter aperture photometry from the version 3.4 public-release SDWFS catalogs, *WISE* will detect ~ 90 sources deg^{-2} with $[3.6] - [4.5] \geqslant 0.5$, of which 90% will reside within the Stern et al. (2005) AGN wedge. Similarly, 90% of sources residing within the Stern et al. (2005) wedge will have $[3.6] - [4.5] \geqslant 0.5$. For comparison, SDSS finds 15 quasars deg^{-2} to $i^* = 19.1$ (Richards et al. 2002). It is thus expected that *WISE* will be a very powerful instrument for studying the cosmic evolution of AGN with minimal bias due to obscuration.

5. SUMMARY

Spitzer/IRAC imaging of 10 deg^2 in Boötes has detected over half of a million infrared sources as part of the SDWFS. Images and catalogs containing the four-band IRAC photometry for these sources are now available online for the community to use. It is anticipated that SDWFS will facilitate a wide variety of extragalactic science; some of the avenues already being explored have been described above. A forthcoming paper (P. R. Eisenhardt et al. 2009, in preparation) details the discovery of ultracool brown dwarf candidates from the SDWFS data set, including the likely identification of T7 and T8 field brown dwarfs. Other projects that are also being actively developed have been described, including a comprehensive study of infrared-variable AGN (S. Kozłowski et al. 2009, in preparation), and an investigation of infrared background fluctuations (A. Cooray et al. 2009, in preparation). These data will soon become publicly available in a format that combines the SDWFS photometry with optical photometry from the NDWFS (Jannuzi et al. 1999). The combined catalogs will facilitate many entirely new applications of the data set from photometric redshift studies to large-scale structure.

This work is based on observations made with the *Spitzer Space Telescope*, which is operated by the Jet Propulsion Laboratory, California Institute of Technology under contract with the National Aeronautics and Space Administration (NASA). Support for this work was provided by NASA through award number 1314516 issued by JPL/Caltech. This research made

Table 26
High Proper Motion Sources

Target	$\langle\mu_{\rm R.A.}\rangle$	$\langle\mu_{\rm Decl.}\rangle$	$B_{\rm W}$	R	I	J	K_s	[3.6]	[4.5]	[5.8]	[8.0]	Notes
J142534.1+325204[a]	−0″.15	−0″.54	...	...	...	...	...	17.83	17.37	16.65	> 15.85	≈ T3 brown dwarf
J142714.2+335959[b]	−0″.31	−0″.21	19.44	...	...	14.89	14.19	13.81	13.75	13.59	13.61	≈ M1
J142723.4+330403	−0″.30	−0″.17	25.48	23.61	23.82	...	...	18.21	16.96	> 16.66	> 15.85	≈ T7 brown dwarf
J143315.5+330838	−0″.05	−0″.35	23.56	19.74	17.77	16.11	15.41	14.98	15.04	14.85	14.90	M5—West et al. (2008)

Notes. Astrometry, used for the nomenclature, is derived from the first-epoch 3.6 μm images (obtained during UT 2004 January 10–14). Proper motions are per year, derived by averaging the epoch 1 to epoch 3 and the epoch 1 to epoch 4 offsets; all four objects are moving in a SW direction. All tabulated magnitudes are Vega-relative total magnitudes. Optical photometry is from the NDWFS ($B_{\rm W}RI$; B. T. Jannuzi et al., in preparation). Near-infrared photometry is from FLAMEX (JK_s; Elston et al. 2006). Mid-infrared photometry is from SDWFS. Non-detections are the average 5σ limits for the relevant bands across the entire field. Near-IR ellipses indicate that FLAMEX has not observed these sources. Assigned T classes are based on measured [3.6] − [4.5] colors in accordance with Patten et al. (2006).

[a] Photometry for this source is heavily affected by the bleed trail from a nearby bright star, but the source appears undetected in the NDWFS imaging.

[b] J142714.2+335959 is saturated in NDWFS R and I. It has $ugriz$ = 21.24, 18.61, 17.09, 16.35, and 15.96 AB mag according to SDSS DR6.

use of Montage, funded by the NASA's Earth Science Technology Office, Computation Technologies Project, under Cooperative Agreement Number NCC5-626 between NASA and the California Institute of Technology. Montage is maintained by the NASA/IPAC Infrared Science Archive. IRAF is distributed by the National Optical Astronomy Observatory, which is operated by the Association of Universities for Research in Astronomy (AURA) under cooperative agreement with the National Science Foundation. Support for M.B. was provided by the W. M. Keck Foundation. The authors thank Andy Gould, whose suggestions improved the manuscript.

Facilities: Spitzer Space Telescope (IRAC)

REFERENCES

Alard, C., & Lupton, R. H. 1998, ApJ, 503, 325
Arendt, R. G., Fixsen, D. J., & Moseley, S. H. 2000, ApJ, 536, 500
Assef, R. J., et al. 2008, ApJ, 676, 286
Barmby, P., Huang, J.-S., Ashby, M. L. N., Eisenhardt, P. R. M., Fazio, G. G., Willner, S. P., & Wright, E. L. 2008, ApJS, 177, 431
Becker, R. H., White, R. L., & Helfand, D. J. 1995, ApJ, 450, 559
Bell, E. F., et al. 2004, ApJ, 608, 752
Berriman, G. B., et al. 2004, Proc. SPIE, 5493, 221
Bertin, E., & Arnouts, S. 1996, A&AS, 117, 393
Bochanski, J. J., West, A. A., Hawley, S. L., & Covey, K. R. 2007, AJ, 133, 531
Bock, J., et al. 2006, New Astron. Rev., 50, 215
Brand, K., et al. 2006, ApJ, 641, 140
Brodwin, M., et al. 2006, ApJ, 651, 791
Brown, M. J. I., Dey, A., Jannuzi, B. T., Brand, K., Benson, A. J., Brodwin, M., Croton, D. J., & Eisenhardt, P. R. 2007, ApJ, 654, 858
Brown, M. J. I., et al. 2006, ApJ, 638, 88
Brown, M. J. I., et al. 2008, ApJ, 682, 937
Bundy, K., et al. 2006, ApJ, 651, 120
Burrows, A., Sudarsky, D., & Lunine, J. I. 2003, ApJ, 596, 587
Cool, R. J. 2007, ApJS, 169, 21
Cooray, A., Bock, J. J., Keatin, B., Lange, A. E., & Matsumoto, T. 2004, ApJ, 606, 611
Cooray, A., et al. 2007, ApJ, 659, L91
Croft, S., van Breugel, W., de Vries, W., Dey, A., Jannuzi, B., & Rottgering, H. 2004, BAAS, 36, 748
Croft, S., et al. 2008, AJ, 135, 1793
Dai, X., et al. 2009, ApJ, 697, 506
de Vries, W. H., Morganti, R., Röttgering, H. J. A., Vermeulen, R., van Breugel, W., Rengelink, R., & Jarvis, M. J. 2002, AJ, 123, 1784
Desai, V., et al. 2008, ApJ, 679, 1204
Devriendt, J. E. G., Guiderdoni, B., & Sadat, R. 1999, A&A, 350, 381
Eisenhardt, P. R., et al. 2004, ApJS, 154, 48
Eisenhardt, P. R. M., et al. 2008, ApJ, 684, 905
El Bouchefry, K., & Cress, C. M. 2007, Astron. Nachr., 328, 577
Elston, R. J., et al. 2006, ApJ, 639, 816
Faber, S. M., et al. 2007, ApJ, 665, 265
Fazio, G. G., et al. 2004, ApJS, 154, 10
Galametz, A., et al. 2009, ApJ, 694, 1309
Gardner, J. P. 1998, PASP, 110, 291
Giavalisco, M., et al. 2004, ApJ, 600, L93
Glass, I. S. 2004, MNRAS, 350, 1049
Gorjian, V., et al. 2008, ApJ, 679, 1040
Hickox, R. C., et al. 2007, ApJ, 671, 1365
Higdon, J. L., Higdon, S. J. U., Willner, S. P., Brown, M. J., Stern, D., Le Floc'h, E., & Eisenhardt, P. 2008, ApJ, 688, 885
Hoopes, C. G. 2004, BAAS, 36, 746
Hora, J. L., et al. 2008, PASP, 120, 1233
Hovatta, T., et al. 2008, A&A, 485, 51
Huang, J.-S., et al. 2007, ApJ, 664, 840
Ivezić, Ž., et al. 2002, AJ, 124, 2364
Jannuzi, B. T., Dey, A., & NDWFS Team, 1999, BAAS, 31, 1392
Kashlinsky, A., Arendt, R. G., Mather, J., & Moseley, S. H. 2005, Nature, 438, 45
Kashlinsky, A., Arendt, R. G., Mather, J., & Moseley, S. H. 2007, ApJ, 654, L5
Kenter, A., et al. 2005, ApJS, 161, 9
Kollmeier, J. A., et al. 2006, ApJ, 648, 128
Lacy, M., et al. 2004, ApJS, 154, 166
Lasker, B. M., et al. 2008, AJ, 136, 735
Lépine, S., & Shara, M. M. 2005, AJ, 129, 1483
Luyten, W. J. 1979, LHS Catalogue. A Catalogue of Stars with Proper Motions Exceeding 0"5 Annually (2nd ed.; Minneapolis, MN: Univ. of Minnesota Press)
Martín, E. L., Brandner, W., Jewitt, D. C., Simon, T., Wainscoat, R., Connelley, M., Marley, M., & Gelino, C. 2001, PASP, 113, 529
McGreer, I. D., Becker, R. H., Helfand, D. J., & White, R. L. 2006, ApJ, 652, 157
Monet, D. G., et al. 2003, AJ, 125, 984
Murray, S. S., et al. 2005, ApJS, 161, 1
Papadakis, I. E., Chatzopoulos, E., Athanasiadis, D., Markowitz, A., & Georgantopoulos, I. 2008, A&A, 487, 475
Patten, B. M., et al. 2006, ApJ, 651, 502
Richards, G. T., et al. 2002, AJ, 124, 1
Sarajedini, V. L., et al. 2006, ApJS, 166, 69
Schuster, M. T., Marengo, M., & Patten, B. M. 2006, Proc. SPIE, 6270, 65
Seymour, N., et al. 2008, MNRAS, 386, 1695
Skrutskie, M. F., et al. 2006, AJ, 131, 1163
Soifer, B. T., Spitzer/NOAO Team 2004, BAAS, 36, 746
Stanford, S. A., et al. 2005, ApJ, 634, L129
Stern, D., et al. 2005, ApJ, 631, 163
Stern, D., et al. 2007, ApJ, 663, 677
Strauss, M. A., et al. 1999, ApJ, 522, L61
Sullivan, M., Hopkins, A. M., Afonso, J., Georgakakis, A., Chan, B., Cram, L. E., Mobasher, B., & Almeida, C. 2004, ApJS, 155, 1
Sullivan, I., et al. 2007, ApJ, 657, 37
Tasse, C., Best, P. N., Röttgering, H., & Le Borgne, D. 2008a, A&A, 490, 893
Tasse, C., Le Borgne, D., Röttgering, H., Best, P. N., Pierre, M., & Rocca-Volmerange, B. 2008b, A&A, 490, 879
Tsvetanov, Z. I., et al. 2000, ApJ, 531, L61
van Dokkum, P. G. 2005, AJ, 130, 2647
West, A. A., Hawley, S. L., Bochanski, J. J., Covey, K. R., Reid, I. N., Dhital, S., Hilton, E. J., & Masuda, M. 2008, AJ, 135, 785
White, M., Zheng, Z., Brown, M. J. I., Dey, A., & Jannuzi, B. T. 2007, ApJ, 655, L69
Woźniak, P. R. 2000, Acta Astron., 50, 421
Zehavi, I., et al. 2005, ApJ, 621, 22